ACCEPTED FOR PUBLICATON IN THE APJ
Preprint typeset using LaTeX style emulateapj v. 04/03/99

arXiv:astro-ph/9911065v1 4 Nov 1999

THE EVOLUTION OF EARLY-TYPE GALAXIES IN DISTANT CLUSTERS I.: SURFACE PHOTOMETRY AND STRUCTURAL PARAMETERS FOR 53 GALAXIES IN THE $Z = 0.33$ CLUSTER CL1358+62[1]

DANIEL D. KELSON[2,3], GARTH D. ILLINGWORTH[3], PIETER G. VAN DOKKUM[4,5], AND MARIJN FRANX[5]

Accepted for publicaton in the ApJ

ABSTRACT

Using wide-field, two-color HST imaging of the cluster CL1358+62 ($z = 0.33$), we derive structural parameters for a large, magnitude-limited sample of cluster members. These structural parameters are combined with accurate velocity dispersions in another paper to investigate the fundamental plane in the cluster. We fit integrated $r^{1/4}$-laws to the integrated surface brightness profiles, and fit two-dimensional $r^{1/4}$-law model galaxies to the images directly. A comparison of the results from the two methods shows that the derived half-light radii, r_e, agree very well, with an *rms* scatter of only 13%. The half-light radii range from approximately 1 to 20 kpc, with a median of about 3 kpc ($H_0 = 65\mathrm{km\,s^{-1}Mpc^{-1}}$, $q_0 = 0.1$).

We investigated the stability of r_e by comparing the $r^{1/4}$-law fits to the half-light radii derived using other commonly used surface brightness profiles. In particular, we fit Sersic $r^{1/n}$-laws (finding the best-fit n ranging between n = 1-6) and superpositions of $r^{1/4}$-law bulges with exponential disks. The half-light radii derived from the best-fit Sersic profiles varied with respect to r_e from the $r^{1/4}$-law fits by only 1% in the median, but with a standard deviation of more than 40% in r_e. For the bulge-plus-disk fits, the derived half-light radii were offset from r_e of the $r^{1/4}$-law fits by 10% in the mean, also showing a large standard deviation of more than 40%. By comparing the fitted half-light radii from the Sersic laws with those derived from the bulge-plus-disk fitting, one also finds a large scatter of 30%. Based on these tests, we conclude that, in general, half-light radii are only measured with a typical accuracy of 30-40%.

While there are large uncertainties in half-light radii, these do not impact the subsequent fundamental plane analysis because the combination $r\langle I\rangle^{0.76}$, which enters the fundamental plane, is extremely stable. The *rms* scatter in $r\langle I\rangle^{0.76}$ is less than 3%, regardless of the form of the profile fit to the galaxies.

By fitting bulge-plus-disk profiles, we find that the median bulge fraction of the sample is 84% and that the few E+A galaxies in this sample have disks which make up about 10-35% of their total light. These results are consistent with the residuals from fitting two-dimensional $r^{1/4}$-law models directly to the galaxies, in which disk-like structures are revealed in about half of the sample. Two of the three E+A galaxies show spiral arm structure.

1. INTRODUCTION

Galaxy scaling relations provide a unique opportunity to study the evolution of stellar populations through intermediate redshifts (Franx 1993, Vogt *et al.* 1996, 1997). Since their discovery (Faber & Jackson 1976, Tully & Fisher 1977), such scaling laws have been used primarily to measure distances, with a reliability seemingly limited only by measurement errors and the homogeneity of the galaxies in question. The Hubble Space Telescope (HST) and WFPC2 have enabled high S/N imaging of intermediate redshift galaxies with a resolution similar to ground-based imaging of galaxies in the Coma cluster. Using the high spatial resolution and S/N of WFPC2, and efficient spectrographs at large aperture telescopes like the Keck 10m, we can directly measure galaxy scaling relations up to redshifts of unity in an effort to understand their origins, and how galaxies evolve (*e.g.*, Schade *et al.* 1997, van Dokkum *et al.* 1998b, Simard *et al.* 1999).

Of the known scaling relations, the fundamental plane (Faber *et al.* 1987, Djorgovski & Davis 1987) has the lowest observed intrinsic scatter, only ~15% in distance for a given galaxy (Jørgensen, Franx, & Kjærgaard 1993, Kelson *et al.* 1997). The fundamental plane (FP) is an empirical correlation between effective radius, r_e, central velocity dispersion, σ, and surface brightness, $\langle I\rangle_e$, for early-type galaxies. In a study of 11 nearby clusters Jørgensen *et al.* (1996) found, in Gunn g,

$$r_e \propto \sigma^{1.16}\langle I\rangle_e^{-0.76}, \tag{1}$$

with a low (*rms*) scatter of $\pm$20% dex in r_e. In Coma, the scatter is even lower, $\pm$14% in distance (Lucey, Bower, & Ellis 1991, Jørgensen, Franx, & Kjærgaard 1993). The fundamental plane of Virgo ellipticals also has a very low internal scatter of $\pm$12% in distance (Kelson *et al.* 1999). Using the virial theorem and assuming that early-type galaxies are an homologous family, the low scatter in the fundamental plane implies a scatter of only $\pm$20% in M/L ratio for a given a galaxy mass.

The utility of the fundamental plane for probing the luminosity evolution of early-type galaxies has been clearly demonstrated by van Dokkum & Franx (1996), Kelson *et al.* (1997), and van Dokkum *et al.* (1998b), who measured the evolution of the fundamental plane zero-point out to $z = 0.83$. The implied evolution of the M/L_V ratios is consistent with a high redshift of formation for stars in early-type galaxies in rich clusters. Projections of the fundamental plane, such as the r-L relation (Ko-

[1]Based on observations with the NASA/ESA *Hubble Space Telescope*, obtained at the Space Telescope Science Institute, which is operated by AURA, Inc., under NASA contract NAS 5–26555.

[2]Department of Terrestrial Magnetism, Carnegie Institution of Washington, 5241 Broad Branch Rd., NW, Washington, DC 20015

[3]University of California Observatories / Lick Observatory, Board of Studies in Astronomy and Astrophysics, University of California, Santa Cruz, CA 95064

[4]Kapteyn Astronomical Institute, P.O. Box 800, NL-9700 AV, Groningen, The Netherlands

[5]Leiden Observatory, P.O. Box 9513, NL-2300 RA, Leiden, The Netherlands

rmendy 1977) and the 1-parameter L-σ Faber-Jackson relation (Faber & Jackson 1976), have also been used by other authors to study early-type galaxy evolution to high redshifts (Schade *et al.* 1997, Ziegler & Bender 1997, Bender *et al.* 1998, Pahre, Djorgovski, & Carvalho 1998).

Other studies of high redshift cluster galaxies have confirmed the notion that early-type galaxies are homogeneous, and likely to be old (Schade *et al.* 1997, Ellis *et al.* 1997). Furthermore, Dressler *et al.* (1997) showed that there has been substantial evolution in the numbers of S0 galaxies between redshifts $z \sim 0.5$ and the present. However, many such results derive from limited imaging of cluster cores. Recently, van Dokkum *et al.* (1998a) used the color-magnitude relation of early-type galaxies to show that the uniformity of age extends to large radii for the ellipticals of CL1358+62, and that the most recent star-formation in massive clusters has occurred in the outer parts, in galaxies with disks. van Dokkum *et al.* showed that the stellar populations of galaxies with disks are less homogeneous than pure bulge systems, but only at cluster radii which are outside the standard WFPC2 footprint (at the distances of intermediate redshift clusters). Evolution in cluster galaxies may be best detected in large, wide-field surveys of clusters: cluster membership, wide spatial extent, and large samples inclusive of all morphological types are all crucial for finding, and measuring the evolution in cluster populations. Surveys which are specifically biased towards ellipticals may miss much of the recent ($z < 1$) evolution in cluster galaxies because the samples are biased against those morphologies which have undergone the most recent epochs of star-formation.

The first detailed study of membership in CL1358+62 was performed by Fabricant *et al.* (1991), who measured a blue and active galaxy fraction of ~15%. Complete membership to $R = 21$ mag is discussed by Fisher *et al.* (1998) and a small subsample was used by Kelson *et al.* (1997) to find the fundamental plane zero-point for the cluster. van Dokkum *et al.* (1998a) has made a complete analysis of the Color-Magnitude relation of 194 confirmed cluster members within the $8' \times 8'$ HST mosaic. The imaging consists of two colors (F606W and F814W) in 12 CVZ pointings. This WFPC2 imaging of CL1358+62 is a superb foundation for building a detailed history of cluster galaxies, from the current epoch, through intermediate redshifts. Future work will concentrate on mosaics of WFPC2 imaging in the clusters MS2053–04 ($z = 0.58$) and MS1054–03 ($z = 0.83$).

Since the publication of Kelson *et al.* (1997), we have completed the surface photometry for a high-resolution spectroscopic sample of galaxies within the HST mosaic's field. This subset of the large membership database will be used for analysis of the fundamental plane and absorption line strength properties. The data are discussed in §2. The photometric calibration, the transformation to redshifted Johnson colors, and sources of systematic calibration errors, are discussed §3. The techniques used to fit $r^{1/4}$-law profiles to the data are discussed at length in §4. In §5 we discuss such instrumental issues as the under-sampling and point-spread function errors. Deviations from the de Vaucouleurs profile are explored at some length in Sections 6 and 7 using $r^{1/n}$-laws (Sersic 1968) and bulge-disk decomposition of the circularized profiles. Tables of the structural parameters are given in §8 and our results are summarized in §9.

2. THE DATA

The HST imaging consists of 12 contiguous pointings, making up a large mosaic of the cluster environment, about $1.5h^{-1}$ Mpc on a side (where $H_0 = 100h$ km s^{-1}Mpc^{-1}). Each pointing consists of three 1200 s exposures in each of F606W and F814W. The data were preprocessed by the standard pipeline procedures which are discussed elsewhere (Holtzman *et al.* 1995).

The analysis presented in this paper was performed on the images processed by van Dokkum *et al.* (1998a), who cleaned the images of cosmic rays, modeled and removed the complicated background, and combined the individual exposures. The most demanding task was the removal of the scattered earth light that resulted from the observations being performed in the Continuous Viewing Zone (CVZ) (see van Dokkum *et al.* 1998a). In some of these observations, the background was higher by factors of two to three. This scattered light increases the counts in the sky background, and the secondary mirror supports cast shadows in the pattern of an "X," in which the background counts are typically not elevated. The excess in the background, and contrast between the shadowed and illuminated regions of the CCDs can vary greatly, and its magnitude depends on the position of the telescope in its orbit when a CVZ exposure is taken. Fortunately, in each set of three exposures, in a given pointing and filter, at least one frame had minimal or no scattered light, thereby allowing accurate modeling of the scattered earth light. Large-order ($n \gtrsim 15$) bivariate polynomials were fit to the background and subtracted. More details of this modeling are given by van Dokkum *et al.* (1998a).

The selection of our fundamental plane sample is discussed in Kelson *et al.* (1999a). Briefly, we randomly selected cluster members within the field of view of the HST mosaic, to $R \leq 21$ mag. The selection was performed to efficiently construct multi-slit plates for the Low-Resolution Imaging Spectrograph (Oke *et al.* 1995). We used three masks, with different position angles on the sky. The region of maximum overlap is in the center of the cluster, and thus the FP sample is concentrated towards the core of the cluster.

Morphology was not a factor in the selection of our sample. In the random selection process, three E+A galaxies were included; these will be compared with those cluster members that have normal, early-type spectra. The sample is about 50% complete for $R \leq 20.5$ mag (see Fisher *et al.* 1998 for details on the statistical completeness of the original redshift catalog). Three galaxies fainter than $R = 21$ mag were added to test the quality of velocity dispersion measurements for faint galaxies. These spectroscopic observations and their reductions are detailed in Kelson *et al.* (1999a). In total, we have central velocity dispersions for 55 galaxies in the cluster. Unfortunately, two of the galaxies were imaged too close to the WFPC2 CCD edges to obtain reliable structural parameters. Thus, there are a total of 53 cluster members in our determination of the fundamental plane in CL1358+62.

Images of these 53 galaxies are shown in Figure 1. The images clearly show a wide range of morphologies, from ellipticals to early-type spirals. Optical morphologies have been taken from Fabricant *et al.* (1999). These authors classified several hundred galaxies in the HST mosaic according to morphological type, T. The galaxies in our high-resolution spectroscopic sample have $T \in \{-5, -4, -3, 0, 1, 2, 3\}$ (E, E/S0, S0, S0/a, Sa, Sab, Sb, respectively). The galaxy morphologies are listed in Table 1, in which there are 11 E, 6 E/S0, 14 S0, 13 S0/a, 6 Sa, 2 Sab galaxies and 1 Sb galaxy. This distribution is quite similar to nearby massive clusters (*e.g.*, Oemler 1974).

3. PHOTOMETRIC CALIBRATION

The aim of this work is to produce surface photometry for use in the analysis of the fundamental plane in the cluster. To enable comparison of the CL1358+62 fundamental plane with equivalent observations of nearby galaxies, the calibrated HST photometry must be transformed to a standard system. Such transformations to a photometric system of redshifted Johnson B and V bandpasses will allow us to compare our observations directly to observations of nearby galaxies. Precisely these transformations and calibration steps have been used previously by Kelson *et al.* (1997) and van Dokkum *et al.* (1998a). Each step has its own uncertainties, which will be summarized at the end of the section.

3.1. *Zero-points*

In this section, we describe the multiple components in the zero-point calibration of the HST photometry in F606W and F814W. The starting points of the calibration are the zero-points for F606W and F814W derived by Holtzman *et al.* (1995) using photometry of stars (point sources) with an aperture of $r = 0''.5$. Our measured surface brightnesses have an effective aperture defined by the extent of our adopted point-spread functions, in this case $r = 1''.5$. Thus, we must correct our magnitudes from the $r = 1''.5$ aperture to an effective aperture of $r = 0''.5$. Using the encircled energy curves in the *HST Data Handbook*, we estimate the correction to be +0.067 mag. The Holtzman *et al.* (1995) calibration is also valid for data taken using a gain of $14e^-$/ADU. Therefore we also incorporate the gain ratios for the individual CCDs as given by the handbook. Furthermore, the HST Distance Scale Key Project has measured a difference of 0.050 mag between long and short exposures of identical fields (see, *e.g.*, Hill *et al.* 1997, Stetson *et al.* 1998) such that long integrations have more counts than would be expected by simply scaling the shorter exposures. Thus, the WFPC2 zero-points, which were derived from short integrations of star fields, are not appropriate for long integrations, and need to be corrected by +0.050 mag.

In summary, the F606W and F814W magnitudes are defined by

$$\mathrm{F606W} = -2.5\log(DN/s) + 21.419 + 2.5\log(GR_i) + 0.067 + 0.050 \quad (2)$$

$$\mathrm{F814W} = -2.5\log(DN/s) + 20.840 + 2.5\log(GR_i) + 0.067 + 0.050 \quad (3)$$

where GR_i represents the ratios of the high- to low-gain modes for the four WFPC2 CCDs, respectively: $1.987, 2.003, 2.006, 1.955$. The total exposure time for each point was 3600 s per filter.

3.2. *Transformation to redshifted V, $(B-V)$*

In order to compare the surface brightnesses and M/L ratios of distant galaxies to equivalent observations made nearby, we must transform the photometry to a consistent system. Towards this end, we define B_z and V_z as the Johnson B and V filter bandpasses redshifted to $z = 0.33$, the observed frame of the galaxies. As one can see in Figure 2, the B_z and V_z bands fall at roughly 5500 Å and 7000 Å, overlapping substantially with the observed F606W and F814W bandpasses. Without the color information, one would be required to extrapolate to, *e.g.*, V magnitude using K corrections. However, we can derive an accurate transformation from the WFPC2 system to the redshifted Johnson system by interpolation using the color information.

As in van Dokkum & Franx (1996), the flux in the redshifted filter can be written as a function of the fluxes in the observed bandpasses:

$$F_{V_z} = F^{a}_{\mathrm{F606W}} \times F^{(1-a)}_{\mathrm{F814W}}, \quad (4)$$

where a is a color term in this transformation (see below). In order to relate the flux in a given bandpass to a standard magnitude, one must use filter constants (see below). Solving for V_z as a function of the observed magnitudes and the filter constants, c_X, finds:

$$V_z = \mathrm{F814W} - c_{\mathrm{F814W}} + c_V + a\left[(\mathrm{F606W}-\mathrm{F814W}) - (c_{\mathrm{F606W}} - c_{\mathrm{F814W}})\right] + 2.5\log(1+z) \quad (5)$$

The additional factor of $2.5\log(1+z)$ compensates for the stretching in wavelength of the redshifted bandpass. The B_z and V_z magnitudes are redshifted measures of the fluxes, not restframe quantities. Removal of the $(1+z)^4$ surface brightness dimming is required to convert these data to magnitudes in the restframe of the galaxies.

The filter constants, c_X, are used to convert the V_z, F814W, and F555W magnitudes to a system of flux units in a given filter. This system can be thought of as similar to an AB system. These constants are defined by $c_X = X - X_{AB}$, where X is the magnitude, through filter X, in the standard system. One can calculate the *AB* magnitudes of Vega in the different filters, and, using the reported magnitudes in the literature for Vega (Holtzman *et al.* 1995), define the transformation from the standard (Johnson) system to an *AB* system, based on absolute flux units. We used the Vega spectrum from Bohlin (1996, Hayes 1985), the filter transmission curves for the WFPC2 filters, and the Johnson filter curves (Bessell 1991), as well as the WFPC2 CCD response curve to determine the *AB* magnitudes of Vega in the various filters. These *AB* magnitudes are zero-pointed to Vega, not the spectra of F dwarfs (*i.e.* AB79, Oke & Gunn 1983; see Frei & Gunn 1994, or Fukugita, Shimasaku, & Ichikawa 1995, Fukugita *et al.* 1996).

Using the SEDs of E/S0 galaxies (Pence 1976), one integrates over the observed and redshifted filter curves to solve for a, for a given SED:

$$a = \frac{(V_z - c_V) - (\mathrm{F814W} - c_{\mathrm{F814W}})}{(\mathrm{F606W} - c_{\mathrm{F606W}}) - (\mathrm{F814W} - c_{\mathrm{F814W}})} \quad (6)$$

to find

$$V_z = \mathrm{F814W} + 0.204 \times (\mathrm{F606W} - \mathrm{F814W}) + 0.652 \quad (7)$$

$$(B_z - V_z) = 0.818 \times (\mathrm{F606W} - \mathrm{F814W}) - 0.128 \quad (8)$$

for galaxies with E/S0 spectra at $z = 0.33$. Using SEDs typical of spirals yield transformations which differ by only ± 0.01 mag. As noted above, these transformations are identical to those used by Kelson *et al.* (1997) and van Dokkum *et al.* (1998a).

3.3. *Colors*

Colors in the WFPC2 filters are taken directly from van Dokkum *et al.* (1998a). They measured (F606W − F814W) colors within r_e for each of the cluster members within the HST mosaic; their color errors (random) are on the order of ± 0.01 mag. For the purposes of the photometric calibration, the absolute color uncertainties should approximately equal the quadrature sum of the two Holtzman *et al.* (1995) zero-point errors. Other effects, such as the exposure time correction, the charge-transfer effect, gain variations and aperture corrections, cancel since they are equal contributors to the calibration of each bandpass. We comment more on color uncertainties below.

3.4. *Galactic extinction*

Galactic extinction has been taken from Burstein & Heiles (1982) and used in conjunction with Cardelli, Clayton, & Mathis (1989) to derive the extinctions in the HST filters. The Burstein & Heiles $E(B-V)$ color excess is 0.006 mag. Using Cardelli *et al.*, we find $R_{\rm F606W}$ = 2.91 and $R_{\rm F814W}$ = 1.94. Thus, $A_{\rm F606W}$ = 0.02 and $A_{\rm F814W}$ = 0.01. Thus, we correct both the measured colors and the redshifted V surface brightnesses by 0.01 mag. Because the Galactic reddening is low in the direction of CL1358+62, reddening uncertainties will contribute little to the following error budget.

3.5. *Uncertainties in the Redshifted Photometry*

Errors in the final calibration of the redshifted V_z-band surface brightnesses can arise from three sources: (1) errors in the HST zero-point calibration, (2) errors in the measured colors, and (3) errors in the transformation from the observed to redshifted bandpasses. We now attempt to summarize these uncertainties, and estimate the total error in our calibrated V_z magnitudes.

Each step in the calibration of HST photometry introduces uncertainties. In the previous section, we showed that the V_z-bandpass is very closely tied to F814W, with a moderate color term. Thus, errors in the Holtzman *et al.* (1995) zero-point for F814W propagates directly to systematic errors in the V_z magnitudes. The F814W zero-point uncertainty is listed by Holtzman *et al.* (1995) as $\pm$0.006 mag. Their calibration, however, is explicitly valid for the spectral energy distributions of stars, so the calibration has larger uncertainties when applied to the SEDs of galaxies, probably on the order of 1-2%. Furthermore, the Holtzman *et al.* (1995) zero-point is valid for $0\farcs5$ radius aperture magnitudes. Our surface brightnesses will have been measured using data deconvolved with a point-spread function with a finite radius ($1\farcs5$). Therefore, we must correct our data from an effective aperture of $r = 1\farcs5$ to an effective aperture of $r = 0\farcs5$. A reasonable estimate for the uncertainty in this correction is $\pm$0.01 mag. Another source of error arises from uncertainties in the Extragalactic Distance Scale Key Project's correction to the zero-point (see, *e.g.*, Stetson 1998); we estimate that it introduces an uncertainty on the order of $\pm$0.025 mag (half the effect).

The color term in the transformation to redshifted V_z is small, with the result that errors in V_z due to uncertainties in the (F606W – F814W) colors are diminished by nearly a factor of five. These color errors include the uncertainty in the F606W zero-point, which we assume to be on the order of $\lesssim$ 0.05 mag, compared to the estimate by Holtzman *et al.* (1995) of $\pm$0.005 mag (the F606W zero-point was determined theoretically, and no additional calibration since Holtzman *et al.* (1995) has been attempted). With regard to the colors, any systematic variations in the CCD gain and charge transfer, for example, cancel. As stated earlier, the error in the adopted Galactic reddening is likely to be small, no greater than $\pm$0.01 mag. Thus, the primary component of systematic error is the F606W zero-point. If the (F606W – F814W) color error can be thought of as the quadrature sum of the Holtzman *et al.* (1995) zero-point errors, then the resulting error in V_z from galaxy colors is still $\lesssim$ 0.01 mag. Color gradients within the galaxies themselves could be a larger factor, but van Dokkum *et al.* (1998a) showed that, in the mean, the colors change very little as one adopts different standard radii for measurement of the colors.

Errors in the coefficients in the transformation come from several sources. Uncertainties in the filter constants are estimated to be $\pm$0.03 mag in the final transformation. Variations in the intrinsic galaxy SEDs lead to (slightly) different values for the color and constant terms in the transformations themselves, introducing an uncertainty of $\pm$0.01 mag. Lastly, adoption of the Hayes (1985) spectrum of Vega may also lead to errors if the WFPC2 photometric calibration sources were not strictly on the same spectrophotometric system as the Hayes spectrum. Unfortunately, the magnitude of this uncertainty is not well known, though we estimate it to be no larger than $\pm$0.05 mag based on the agreement of several sources of filter constants with with Holtzman *et al.* (1995).

By adding these contributions in quadrature, we estimate a total error of $\pm$0.06 mag in V_z and $\pm$0.05 mag in $(B_z - V_z)$ color. For the analysis of the fundamental plane, these uncertainties can be treated as systematic errors.

4. FITTING DE VAUCOULEURS PROFILES

The photometric parameters, r_e and $\langle I \rangle_e$, were obtained by fitting $r^{1/4}$-law profiles to the galaxies and two distinct approaches were used to fit $r^{1/4}$-laws to the data. The first approach involved restoration of the data (deconvolution) using the CLEAN procedure (Högbom 1974), isophote fitting using GALPHOT (Jørgensen *et al.* 1992), the derivation of a circularized, integrated surface brightness profile (*i.e*, a "growth" curve), and its fit with an integrated $r^{1/4}$-law.

The second approach involved fitting two-dimensional galaxy models to the images directly (cf. van Dokkum & Franx 1996). The algorithm involves convolving two-dimensional $r^{1/4}$-laws with a PSF, iteratively adjusting the parameters until the model provides a good fit to the WFPC2 images. Nearby, contaminating objects can be handled elegantly, since multiple objects can be fit simultaneously (see also Simard 1998). For both of these procedures we used artificial PSFs for each galaxy. These PSFs were created using Tiny Tim 4.0b (Krist 1995). We estimate the effects of PSF errors in §5.

4.1. *Fitting Integrated Surface Brightness Profiles*

In this section, we discuss the procedures used for fitting the integrated profiles derived from the WFPC2 images. Before deriving the surface photometry, the images must be deconvolved because the structural parameters r_e and I_e can be seriously affected by the WFPC2 PSF and its broad wings. We chose to use the CLEAN method of deconvolution because it is fast, efficient, and simple (Högbom 1974). The output images were convolved with a Gaussian smoothing function to reduce the noise in the output image. The residual maps typically contained $\lesssim$ 1% of the counts in the original image but were nevertheless added to the output frames in order to preserve flux. We fitted elliptical isophotes using the program GALPHOT (Jørgensen *et al.* 1992). The radii were spaced logarithmically, with an inner isophote radius of r = 0.3 pixels, extending out to radii typically five times larger than r_e.

In deriving structural parameters for our galaxies, we duplicated the procedures used on nearby galaxies, fitting the integrated profiles rather than the profiles themselves.

4.1.1. *Fitting for r_e*

The flux in the CLEANing process has been restored with an effective PSF, chosen to be a Gaussian with FWHM $\equiv$ 1 pixel. At any given radius, one needs to correct the analytical $r^{1/4}$-law growth curve for the convolution by the restoration PSF.

The enclosed flux within a given radius for an $r^{1/4}$-law profile is analytically simple:

$$F(r) = \pi r_e^2 I_e \frac{8e^{7.676}\gamma(8,x)}{7.676^{-8}}, \quad (9)$$

$$= \pi r_e^2 \langle I \rangle_e \frac{2\gamma(8,x)}{7!}, \quad (10)$$

$$x = 7.676\left(\frac{r}{r_e}\right)^{1/4}$$

The least-squares fit can be linearized straightforwardly, since the derivatives of Equation 11, with respect to r_e and I_e (or $\langle I \rangle_e$), are also analytically simple.

For a given set of structural parameters (r_e, I_e), one can readily compute how much interior flux should be redistributed outside of a given radius in the growth curve. In this fashion, one adjusts the growth curve due to the smearing by the restoration PSF (see, *e.g.*, Saglia *et al.* 1993). At each radius, one computes a set of aperture corrections to correct the model to a "seeing"-convolved model (assuming circular symmetry). These corrections are determined numerically for each set of structural parameters tested in the search for χ^2 minimum. The expression for the convolved model growth curves is

$$G(r) = \int_0^\infty \int_0^\infty 2\pi\rho I(\rho) P(k) J_0(kr) J_1(k\rho) dk d\rho \quad (11)$$

where the restoration PSF is described by its transform, $P(k)$, and J_0 and J_1 are zeroth and first order Bessel functions. For $I(\rho)$, we use the fitted profile. We use the Levenberg-Marquardt method to perform the χ^2 minimization, fitting $G(R)$ to the integrated surface brightness profiles.[6] Once the set of structural parameters has been found which minimizes χ^2, we have r_e, I_e, and $\langle I \rangle_e$ for the fitted model. Once the model has been fit, the galaxy profile may not be perfectly fit by the model within r_e, the radius within which $\langle I \rangle_e$ is defined. Therefore, we use the observed $\langle I \rangle_e$, *i.e.*, the enclosed flux within r_e for the observed profile instead of the enclosed flux for the model, and have corrected this surface brightness for the smearing effects of the restoration PSF (see Equation 11). Using either the observed or model $\langle I \rangle_e$ has an effect on $r_e \langle I \rangle_e^{0.76}$ of less than 0.1% in the mean.

In Figure 3, we show the calibrated F814W surface brightness profiles and integrated surface brightness profiles. The fit by the integrated de Vaucouleurs profiles are shown by thick solid lines in the right-hand panels. The implied $r^{1/4}$-law profiles are shown in the left-hand panels. The residuals are shown in the lower panels, using thick solid lines as well. In general, the quality of the fit to the integrated profiles is good.

4.1.2. *Sensitivity to Fitting Range*

In the fitting process, one must select a range of radii over which to fit the integrated surface brightness profiles. At small radii, the profile shapes are affected by PSF errors which may have been exacerbated by the (de)convolution procedures. Secondly, at large radii the profiles themselves become noisy, and thus the growth curve shapes can become suspect.

Three effects limit the choice of inner radius in the fit: (1) the CLEAN procedure may not be perfect and noiseless; (2) the Tiny Tim construction of the WFPC2 PSF may not be perfect; and (3) the correction for the smearing by the restoration PSF may not be perfect. These effects are exacerbated by the under-sampling of the data.

The outer radius was chosen in order to minimize the effects of sky-subtraction errors. The shape of a galaxy's outer profile can be greatly affected by errors in the sky background, even though fitting of a parameterized growth curve is intended to be robust against such uncertainties.

We find that the results are quite stable to the choice of inner and outer fitting radii. We varied the outer fitting radius between 2.0, 2.5 and $3r_e$, and the inner fitting radius between 0, 0.5, 1 pixel, and 2 pixels. (For $H_0 = 65$ km s^{-1}Mpc^{-1} and $q_0 = 0.1$, one WFPC2 pixel corresponds to 0.48 kpc, equivalent to $1''$ at the distance of Coma.) For all combinations of the fitting range, mean and median differences in r_e are less than $\pm 1.5\%$. We found that $2r_e$ was a suitable compromise for the outer radius in fitting the growth curve. After investigating the uncertainties due to PSF errors and the under-sampling (§5), we adopted an inner fitting radius of $r = 1$ pixel.

In the extreme case, changing the inner and outer fitting radii to $r = 0$ and $r = 3r_e$, the mean systematic offset in r_e is about 1%, with an *rms* scatter in the r_e values of 9%. The systematic offset in $r_e I_e^{0.76}$, the combination of the structural parameters which appears in the fundamental plane, is negligible, with an *rms* scatter of 0.1%. The stability of the effective radii to the inner fitting boundary gives us confidence that the procedure outlined above properly corrects for the convolution by the restoration PSF.

4.1.3. *Sensitivity to Sky Subtraction*

One important source of error not addressed by varying the inner and outer fitting radii was uncertainties in the determination of the sky background. When the imaging data were processed in van Dokkum *et al.* (1998a), the background was modeled and subtracted using order $n \gtrsim 15$ polynomials. However, for any given galaxy there may still be residual background fluctuations that were not accurately removed by the modeling. Thus, we followed the procedure in Jørgensen *et al.* (1992), where low-order power laws ($m = 2, 3$) are fit to the outer parts of the profiles using an unweighted least-squares routine. The sky value is estimated from the asymptotic convergence of $I = I_0 r^{-m} + \text{sky}$.

The *rms* scatter in extrapolated sky values was $5e^-$ (~24 mag/$\square''$). By ignoring this fit for the local background, the effect on r_e is about 1%, in the mean, with a standard deviation of 3%. No effect on the fundamental plane parameters was found.

In summary, the fundamental plane parameters derived from the fitting of the integrated profiles, for all combinations of the inner and outer fitting radii, are extremely robust against the choice of fitting range. The insensitivity to the fitting range and to uncertainties in the sky subtraction suggest to us that the growth-curve parameters are well-determined.

4.2. *Fitting the Images Directly*

In this section, we derive structural parameters by fitting two-dimensional model galaxies directly to the WFPC2 images (see van Dokkum & Franx 1996 for a discussion of the technique used here, and other authors for variants of the method *e.g.*, Schade *et al.* 1997, Simard 1998). Images of model galaxies,

[6] In order to linearize the fitting procedure, we continue to describe the growth curve's derivatives by their analytical expressions, multiplied by the ratio of $G(R)/F(R)$, where G and F are the convolved and unconvolved values of the cumulative flux.

for a given set of structural parameters, are convolved with the Tiny Tim PSFs and compared directly to the data frames. The structural parameters are adjusted until χ^2, or some other measure of the goodness of fit, is minimized. The local topology of χ^2 is generally used to estimate the uncertainties in the fit.

Procedures for fitting the images directly have the advantage that one performs a convolution rather than deconvolution. The advantages of such a process include the preservation of the image's noise characteristics, and the fitting of multiple objects simultaneously. The current disadvantage is that the 2D models are built using a single, global ellipticity and position angle for each galaxy. Nonetheless, as the apparent information content continues to shrink with the decreasing angular sizes of high redshift galaxies, useful structural parameters are still extractable via such modeling, so long as the PSF is reasonably well known.

Such fitting methods assume a functional form to the galaxy profile, such as an $r^{1/4}$-law, but can be expanded to include multiple components (*e.g.*, $r^{1/4}$-law bulge plus exponential disk). The parameters of the least-squares fit to an $r^{1/4}$-law are: (1) (x,y) position of the center; (2) ϵ, the apparent ellipticity; (3) position angle; (4) effective radius; (5) surface brightness at the effective radius; and (6) the sky background. Multiple-component (*e.g.*, bulge-plus-disk) fits require additional parameters and complicated minimization algorithms, but even such expanded profile shapes do not yet take into account deviations from purely elliptical isophote shapes, or twisting of the isophotes with radius.

Using the fitting procedure of van Dokkum & Franx (1996), we derived the $r^{1/4}$-law structural parameters for the galaxies. Given the potential uncertainties in the processing of the sky background in the CCD images, we performed the fitting first with the sky background fixed at zero, and a second time while fitting for the local sky background. When the sky background is fit, the r_e changes by a mean (median) of +2% (+0.1%), with a scatter of nearly $\pm$10%. The additional fitting of local sky has a negligible effect on the fundamental plane parameter in the mean ($<$ 0.1%), with a scatter of 0.5%. For some galaxies, r_e could change by as much as 30-40%, but even for these extreme cases the fundamental plane parameter only changes by $\lesssim$ 2%.

In Figure 4, we show the galaxy images, after subtraction with the best-fit 2D $r^{1/4}$-law models. Many disk-like structures are clearly visible in these residuals and bulge-plus-disk fits to the 1D profiles are discussed in §7.

4.3. *Comparison of Growth Curve and Image Modeling*

Ideally the two fitting procedures should yield similar, or even identical structural parameters. In practice this will not be the case for several reasons. For example, the two procedures have intrinsically different weighting schemes in the fitting process. Furthermore, galaxies do not have surface brightness profiles which obey perfectly an $r^{1/4}$-law, or any other simply parameterized function. While the internal tests listed above, such as varying the fitting range of the integrated surface brightness profiles, or allowing the image modeling to fit the sky background, help estimate some of the uncertainties in the measurements, the methods themselves suffer from their own systematics. Therefore, we now compare the structural parameters derived from the two methods in order to help estimate remaining systematic uncertainties.

The comparison of effective radii derived by the two algorithms is surprisingly good, considering the range of apparent morphologies covered by the sample. The median difference in effective radii between the two algorithms is only 1%. The standard deviation is 13% in r_e, precisely the quadrature sum of the *rms* scatter derived in the individual internal tests. The median offset in effective surface brightness is –4%. Thus, there is a systematic offset in the effective fundamental plane parameter of 1.5%, with a standard deviation of 2.5%. Nominally, one would expect that the error in the fundamental plane parameter should be smaller than the error in the individual structural parameters, because of the correlation between r_e and surface brightness. However, the two fitting methods weight the data differently and are therefore affected differently by the under-sampling and PSF errors, which are addressed in the next section. Nevertheless, these results indicate that the errors in the fundamental plane parameters are small.

5. REMAINING INSTRUMENTAL EFFECTS

While the above tests show that the fundamental plane parameters appear well constrained, there are potential sources of error in common to both methods. The two most important effects are (1) the under-sampling; and (2) the use of model point-spread functions. Even those these effects are common to both methods, the data are weighted differently in the χ^2 calculation. As a result, the two fitting methods are not affected identically.

5.1. *The Effects of Under-sampling*

In order to test the effects of under-sampling, and the dependence of the PSF on sub-pixel positioning, we generated a 10$\times$ subsampled Tiny Tim PSF. We created a set of noiseless subsampled $r^{1/4}$-law galaxy images using the subsampled PSFs. We then created two sets of WF CCD sampled versions of these model galaxies. The first set were simply block-averaged to the nominal WF CCD sampling and convolved with a charge-smearing kernel (Krist & Hook 1997). Thus, the galaxy centroids were located at the precise corner of a WF CCD pixel. The second set were created by shifting the subsampled model galaxy images by 0$''$.05 (half a WF CCD pixel), then block-averaged, and convolved with the charge-smearing kernel. In each case, the block-averaged subsampled PSFs are equivalent to the (under-)sampled, real ones. Thus, we had two sets of model galaxy images which differed in position by half a WF CCD pixel. We then used the nominally sampled Tiny Tim PSF, centered at the integer pixel location, to derive structural parameters for these galaxies.

The model images were analyzed in the same manner as the CL1358+62 galaxies, as described in §4.1 and §4.2. The systematic errors in r_e varied with galaxy size, as did the errors in $r_e I_e^{0.76}$. For r_e = 4 pixels, the error in the fundamental plane parameter was only –2%. For r_e = 2 pixels, the error is –5%. For these tests, we restricted the growth curve fitting to radii $r > 1$ pixel. By fitting to the very center, the systematic error in $r_e I_e^{0.76}$ was nearly –10% for galaxies as small as r_e = 2 pixels. Even by directly fitting the images with the two-dimensional models, the derived structural parameters are susceptible to errors due to the under-sampling. For galaxies with r_e = 1 pixel, the systematic errors due to under-sampling can be as large as ~50% in r_e, and $\lesssim$ 10% in $r_e I_e^{0.76}$. Fortunately, the smallest galaxy in our sample has $r_e \approx 2$ pixels; the median effective radius is $r_e \approx 6$ pixels. Therefore, we anticipate that the net systematic effect of the under-sampling on the fundamental plane is small, being 1-2% on average.

We caution against fitting profiles or growth curves too close to the centers of galaxies, even when deconvolution of the

WFPC2 images has taken place, because the under-sampling makes fitting small galaxies quite problematic. Techniques which improve the sampling, such as "drizzling" (Hook & Fruchter 1997) should improve the usefulness of the data for such objects.

5.2. *A Comparison of Stellar and Model Point-Spread Functions*

In both procedures, we have relied on the assumption that the Tiny Tim point-spread function (Krist 1995) is an accurate match to the PSF of the observations. Even when this assumption is be correct for a single exposure, the process of combining multiple exposures in each pointing introduces extra "jitter" in the PSF of the resulting image. The situation is actually worse because one has only a finite number of images, *e.g.*, $N = 3$, and not the limit of $N \to \infty$ images. Therefore the individual jitter vectors are not going to be isotropically distributed, for each galaxy (or star) in a given pointing.

Therefore, we tested to what extent our results are effected by errors in the model PSF. We built model galaxy images using a bright star as the *observed* PSF, and then analyzed these images using a Tiny Tim model PSF. The star was located at approximately $(550, 541)$ in CCD #4 of pointing #1. We performed this test using observed stellar and Tiny Tim PSFs with $1''.5$ diameter.

We generated a $10\times$ subsampled model PSF at the integral pixel location of the star, shifted and resampled it to the pixel size of the WF CCDs, and then convolved with the charge-smearing kernel. We measured the flux-weighted centroid of this nominally sampled PSF and adjusted the sub-pixel shift until its centroid coincided with that of the star. The effects due to under-sampling in the star and Tiny Tim point-spread functions should cancel out, because they are positioned at identical sub-pixel locations (to within 5% of a pixel).

We created a set of 2D model galaxy images which had been convolved with the stellar image. The models had pure $r^{1/4}$-law profiles with effective radii $r_e \in (1, 2, 4, 8, 16)$ pixels. Using the sub-pixel shifted Tiny Tim PSF, we then measured the structural parameters of the model using the direct image fitting. The measured effective radii underestimated the correct values by 17%, 12%, 8%, 6%, and 4%, respectively. This suggests that the model PSF was broader than the star, but because of the under-sampling, this difference in width was not initially obvious. The fundamental plane parameters were systematically larger by 6.8%, 3.6%, 1.8%, 0.8%, and 0.2%, respectively. These offsets are independent of model ellipticity.

The smallest galaxy in our sample has an effective radius of $r_e \approx 2$ pixels ($0''.2$). The median half-light radius of the sample is $0''.6$, with 25 and 75 percentiles of $0''.35$ and $\sim 1''$. Thus, for the upper half of the sample, the uncertainties on the fundamental plane parameters, due to improper matching of the point-spread functions, are $\lesssim 1\%$. For the 25% of the sample with $0''.35 < r_e < 0''.6$, the effects are $\lesssim 3\%$. For the remainder, the uncertainty is $< 4\%$. For galaxies at higher redshift, or for galaxies farther down the luminosity function, one must take extreme care to match the point-spread function to the data, given the potentially large systematic uncertainties at $r_e \approx 1$ pixels.

Using two distinct fitting methods, we have reliably derived effective radii and surface brightnesses. The uncertainties in the effective radii of the de Vaucouleurs profile fits are small, at the level of ~13% *rms*, with a mean offset of only 1%. The measurements are robust against fitting range, uncertainties in the sky background, and fitting method. The uncertainties in the fundamental plane parameters themselves is even smaller, ~2.5% *rms*, with potential systematic uncertainties at the level of $\lesssim 3\%$, due to errors in the PSF, under-sampling, and differences between the fitting methods.

However, other sources of uncertainty in half-light radii may persist, due to deviations in galaxy profiles from the $r^{1/4}$-law form. Therefore, we continue with a discussion of systematic deviations from the $r^{1/4}$-law.

6. SERSIC $R^{1/N}$-LAW PROFILES

The actual surface brightness profiles of galaxies often deviate from pure $r^{1/4}$-laws. In the sample presented here, both bulge and disk components are readily visible in many of the images (see Figures 1 and 4). We now investigate the fitting of more generalized surface brightness profiles to our data to test (1) if a more complex profile is better suited to the profiles of the CL1358+62 galaxies; (2) if such departures from an $r^{1/4}$-law are important for the determination of their structural parameters; and (3) if they allow for accurate and objective morphological classification.

In this section, we generalize the parameterization of the surface brightness profiles to the $r^{1/n}$-law (Caon, Capaccioli, D'onofrio 1993, Graham & Colless 1997), where n, in the case of this paper, is restricted to the set of integers $n \in \{1 \ldots 6\}$. Note that the case of $n = 1$ corresponds to an exponential disk, and $n = 4$ is equal to the de Vaucouleurs profile.

The inclusion of n serves two purposes. First, the best-fit n is a a quantitative descriptor of galaxy morphology. Graham *et al.* (1997) found that the giant cluster ellipticals and BCGs follow $n > 4$ profiles. Furthermore, Saglia *et al.* (1997) showed that $r^{1/n}$ is equivalent to a subset of bulge-plus-disk models, though the relationship between n and B/D is not a straightforward one.

6.1. *Fitting the Growth Curves*

Integrated $r^{1/n}$-laws, with $n = 1, 2, 3, 4, 5, 6$ have been fit to the growth curves of §4.1. The enclosed flux within a given radius for an $r^{1/n}$-law profile can be simply expressed:

$$F_n(r) = \pi r_n^2 \langle I \rangle_n \frac{2\gamma(2n, x)}{(2n-1)!}, \qquad (12)$$

$$x = (2n - 0.324)\left(\frac{r}{r_n}\right)^{1/n}$$

where r_n refers to the half-light radius of the corresponding $r^{1/n}$-law fit. Fundamental plane parameters will be expressed as $r_n I_n^{0.76}$ and $r_n \langle I \rangle_n^{0.76}$.

As in the case of the de Vaucouleurs fitting ($n = 4$), we adopt structural parameters derived from an inner fitting radius of 1 pixel, and an outer radius of $2r_n$. We tested the structural parameters from these fitting functions with direct image model fitting using the $r^{1/n}$-laws for a restricted set of n ($n = 1 \ldots 4$). Comparisons of the structural parameters derived from the image and growth-curve fitting for $n = 1, 2, 3$ were similar to the comparisons for $n = 4$ discussed in §4.3 (in which differences in $r_4 I_4^{0.76}$ were 1.5% in the mean, with 2.5% *rms* scatter).

6.2. *A Comparison of the $r^{1/n}$ Profiles*

By expanding our growth curve fitting to a range of profile shapes, one expects to gain additional knowledge about the

galaxy sizes and morphologies. In this section, we investigate whether or not the new measures of half-light radii are necessarily more accurate than those obtained with the de Vaucouleurs profile. Figure 5(a) shows the distribution of the ratio r_n/r_e (where $r_e = r_4$) using the best-fit n for a given galaxy. This distribution is quite broad, suggesting that the fit of a pure de Vaucouleurs profile can lead to large errors in half-light radius, similar to what has been found for nearby samples (Caon, Capaccioli, D'onofrio 1993).

For a given n, the ratio of r_n/r_4 appears to be a well defined function. As shown in Figure 6(a), $\ln(r_n/r_4) \approx -1.32 + 0.33n$, almost irrespective of the true shape of the galaxies, with a scatter of less ~5%. Thus, the fit of an $n = 6$ profile to an intrinsically $n = 2$ galaxy will find too large a half-light radius by nearly a factor of three. As a result, a large bulk of an $n = 6$ profile is fit to parts of the growth curve which are more susceptible to errors in the sky subtraction. In crowded regions, where a large source of systematic error is the background determination, residual background light can easily appear as a shallow envelope in the integrated surface brightness profiles, masquerading as the profile of an $r^{1/6}$-law, or worse yet, even larger values of n. Of course, the other extreme is also possible. By over-estimating the sky, one can effectively decrease the n derived for a given galaxy. Therefore, when expanding the profile fitting to include the overall shape (n), one must treat the background subtraction with care.

While for fixed values of n, the individual parameters of r_n and I_n are not particularly sensitive to errors in background subtraction (see the earlier case of $n = 4$), the chief uncertainty is *which* value of n to assign to a given galaxy. By varying the range of radii over which one compares the different $r^{1/n}$ fits, one begins to test the sensitivity of n to the uncertainties in sky subtraction. A 3% error in sky subtraction (§4) can lead to changes in n, $\Delta n \approx 1$, and errors in half-light radius of 20-30%. The typical scatter introduced in n due to the sky extrapolation alone is of order $\Delta n \approx \pm 0.2$. Nearly a third of the sample, however, have Δn values larger than this, and many of these are the $n \gtrsim 4$ galaxies for which uncertainties in n on the order of unity are not uncommon. We adopt Δn as the uncertainty in the measurement of n, and the faintest galaxies, as expected, tend to have the largest uncertainties. We conclude that the $r^{1/n}$-law does not yield more accurate estimates of half-light radii, especially for galaxies fit by $n > 4$.

Several authors have commented upon a trend of galaxy shape parameter, "n," with galaxy size (Caon, Capaccioli, D'onofrio 1993, Graham & Colless 1997). However, in Figure 6(a) we saw that the ratio of r_n/r_4 scales in a well-defined manner. By fitting a low-n profile to a galaxy, one will automatically find a smaller half-light radius than when fitting a larger n profile. The half-light radii from low-n fits are simply smaller than the half-light radii one derives when fitting larger-n profiles, independent of the true shape of the galaxy profile. This bias may complicate the nature of the trend of n with galaxy size.

6.3. *Effective and Mean Effective Surface Brightness*

Ideally, the fundamental plane should be insensitive to the detailed profiles of (early-type) galaxies. However, the fundamental plane parameter constructed with the surface brightness at an effective radius is not robust. As can be seen from Figure 6(b), the ratio of $r_1 I_1^{0.76}$ to $r_6 I_6^{0.76}$ is a factor of ~2.5. The ratios of the $r_n I_n^{0.76}/r_m I_m^{0.76}$ to each other are *independent of the real shapes of the galaxy profiles*, to better than a few percent. In Figure 6(c), however, we see that the fundamental plane parameter constructed with the *mean surface brightness* (within r_n) is much more robust with respect to n, showing only ~10% peak-to-peak difference in $r_n \langle I \rangle_n^{0.76}$. The typical scatter about this relation is only a few percent.

The ratio of $r_n \langle I \rangle_n^{0.76}$ to $r_4 \langle I \rangle_4^{0.76}$ is virtually independent of galaxy profile as well. This indicates that every $n = 2$ galaxy fit by a de Vaucouleurs profile is actually measured incorrectly in precisely the same way as every other $n = 2$ galaxy, independent of galaxy size.

In summary, the fitting of the Sersic $r^{1/n}$-law profiles does not lead to more accurate photometric parameters for the purposes of fundamental plane analysis. The derived half-light radii are correlated with the best-fit n, which is sensitive to errors in the sky background. Fortunately, the fundamental plane is insensitive to these uncertainties in the photometric parameters, because the fundamental plane parameters, when constructed using mean effective surface brightnesses, remain constant at the level of 3%.

7. BULGE/DISK DECOMPOSITIONS AND QUANTITATIVE MEASURES OF MORPHOLOGY

Classifying galaxies by morphology becomes increasingly difficult at high redshifts. Distant galaxies are typed using images taken with (linear) CCD detectors, while nearby samples have been primarily typed using (non-linear) photographic plates. Furthermore, the distant galaxies typically span fewer resolution elements, and the images have poorer S/N than images of the nearby prototype elliptical and lenticular galaxies with which we wish to make comparisons. In order to maximize the use of our data in determining galaxy morphologies, we classify the galaxies in our sample by both visual and quantitative morphology. The visual classifications have been taken from Fabricant *et al.* (1999).

In the previous section, we derived the n parameters for the galaxies in our sample. As stated earlier, the Sersic (1968) n profiles are a "restricted" subset of bulge-plus-disk models (Saglia *et al.* 1997). In fitting the growth curves, the use of n as a descriptor of morphology is formally more robust than bulge-disk decompositions. One needs only three quantities to describe a profile, (n, r_e, I_e), rather than four, $(r^B_{1/2}, I^B_{1/2}, r^D_{1/2}, I^D_{1/2})$.

In this section, we test whether n reasonably reflects B/D ratios for our sample of galaxies. To this end, two-component, bulge-plus-disk growth curves were fit to the integrated surface brightness profiles of our galaxies, using the same fitting radii as above. The growth curves were fit between 1 pixel ($0''.1$) and $2r_n$, defined by the "best" fit $r^{1/n}$-law (above). As in the fitting of the $r^{1/4}$-law growth curves, we used the Levenberg-Marquardt method to search for the parameters which minimized χ^2, taking extra care to avoid local minima.

In Figure 3, we show the fitted bulge-plus-disk superpositions and the residuals from this fit using thin solid lines. As is shown in the figures, the galaxies in our sample appear to be well described by the superpositions of de Vaucouleurs bulge ($n = 4$) and exponential disk ($n = 1$) profiles. The individual bulge and disk components are plotted as dashed and dotted lines, respectively. Note that the bulge-plus-disk models tend to provide better fits than a pure $r^{1/4}$-law. The addition of an exponential disk improves the fit for many of the galaxies. The E+A galaxies, ID # 209, 328, and 343, are bulge-dominated, but clearly have disks at the level of 10-35%. Over the entire sample, the median bulge fraction is 84%. Upon visual in-

spection of Figure 4, one finds disk-like structures in about half of the sample, consistent with the visual classifications. Spiral arms are also plainly visible in many, including two of the E+A galaxies.

In many of the galaxies, there appears to be evidence for central exponential (disk) structures. Most of the galaxies with larger bulge fractions show evidence for central exponential components in their surface brightness profiles. This does not appear to be an artifact of the fitting procedures or errors in the PSF, as many of these central "disk" components persist at radii $r \gg 1$ pixel. Evidence of such structures might appear in the kinematic profiles but seeing would complicate the interpretation of such data (Kelson *et al.* 1999a). A full study of the entire membership catalog using two-dimensional model fitting of the images (Tran *et al.* 2000), would help confirm whether this abundance of central exponentials is the norm, or an artifact of the deconvolution process.

Table 1 lists the optical morphologies (Fabricant *et al.* 1999) with the best-fit n parameters. We list (1) galaxy ID, (2) visual morphology, T, from Fabricant *et al.* (1999), (3) $(B-V)$ color, also from van Dokkum *et al.* (1998a), (4) r_e, (5) $\langle\mu\rangle_e$, (6) $r_e\langle I\rangle_e^{0.76}$, (7) n, (8) $r_{1/2}^n$, (9) $\langle\mu\rangle_{1/2}^n$, and (10) $r_n\langle I\rangle_n^{0.76}$. The fundamental plane parameters have been expressed using units of kpc and $L_\odot/\mathrm{pc}^2$ ($H_0 = 65$ km s^{-1}Mpc^{-1}, $q_0 = 0.1$).

Table 2 gives the best-fit bulge fractions for the galaxies in this sample, and lists the individual values of (3) $r_{1/2}$, (4) $\langle\mu\rangle_{1/2}$, (5) $r_{1/2}\langle I\rangle_{1/2}^{0.76}$, (6) $r_{1/2}$ for the bulge component, (7) $\langle\mu\rangle_{1/2}$ for the bulge component, (8) $r_{1/2}$ for the disk component, (9) $\langle\mu\rangle_{1/2}$ for the disk component, Bulge Fraction within (10) $r \leq 0''.2$, (11) $r \leq 0''.5$, and (12) $r \leq 2r_{1/2}$, (13) total bulge fraction, and (14) luminosity-weighted ellipticity, are given for each galaxy. Scale lengths are listed in arcsec, and surface brightnesses in V_z mag/$\square''$. The tables include only formal errors and do not include other sources of errors, such as uncertainties in the calibration or errors due to PSF mismatch.

There were two explicit reasons for expanding the form of the fitted surface brightness profiles to the $r^{1/n}$-laws and bulge-plus-disk superpositions; they are to (1) determine accurate measures of half-light radii; and (2) objective morphological classifications. Earlier we compared the half-light radii from the Sersic profiles to those derived using the de Vaucouleurs profile. In Figure 5(b), we show the distribution of bulge-plus-disk half-light radius, r_{B+D}, divided by r_e, the half-light radius of the de Vaucouleurs profile fit. The distribution is broad, and with Figure 5(a), should further caution the reader about the reliability of half-light radii in general.

The other reason behind expanding the model surface brightness profiles to Sersic profiles, and bulge-plus-disk superpositions was to test whether these forms could be used to objectively classify the galaxies, given the recent interest in quantitative morphologies. In Figure 7, we compare visual and quantitative estimates of morphology to help test their reliability. Figures 7(a-c) compare BF, the bulge fraction of total light, n, the best-fit $r^{1/n}$-law, and ϵ, the flux-weighted apparent ellipticities from the image modeling to the visual classifications, T, of Fabricant *et al.* (1999). In general, the visually classified E/S0s ($T \leq -3$) have high bulge fractions. Those galaxies with $n \geq 4$ are all of type S0/a and earlier. While T and n are clearly correlated, the relationship between profile shape, n, and visual morphology has large scatter. Figure 7(d,e) shows BF and n as functions of ϵ. In Figure 7(f) one sees that galaxies with $n \gtrsim 4$ typically have high bulge fractions. Clearly the relationship between bulge fraction, n, and optical morphology is not straightforward. That there appears to be no tight relation between n and BF, however, should not be surprising. Saglia *et al.* (1997) showed that n is a complicated combination of the bulge fraction and the ratio of disk to bulge half-light radii. We conclude that there is only a level of correspondence between the different estimates of morphology which allows one to discriminate between bulge-dominated and disk-dominated galaxies. It is clear from the figures that these quantitative measures are not successful at distinguishing subtle differences between adjacent morphological classes (*e.g.*, Es from S0s).

8. SUMMARY OF THE STRUCTURAL PARAMETERS

The primary goal of this paper is to provide the photometric parameters required to compare the fundamental plane in CL1358+62 to that measured locally. We have shown that the growth-curve structural parameters are consistent with those derived from directly fitting 2D models to the images.

However, the direct image fitting implemented by van Dokkum & Franx (1996) is currently restricted to rather simple galaxy models: a single component with constant ellipticity and position angle. Other, more sophisticated algorithms, such as those described by Simard *et al.* (1997), could be used as well. Given the magnitudes of the uncertainties in half-light radii (cf. Figure 5), the more sophisticated methods will not likely result in more accurate half-light radii, but simply in greater accuracy in the estimation of their errors. More distant galaxies, with smaller angular sizes, will require more sophisticated modeling to avoid serious systematic errors in structural parameters due to the under-sampling. Despite these issues, we have shown that the measurements of $r_e\langle I\rangle_e^{0.76}$ are quite robust.

The current errors in the structural parameters, as deduced by the differences in the results of our two methods, give us confidence that more complicated procedures would not greatly improve on the analysis. What we do find, however, is that one can use n to *grossly* distinguish between bulge- and disk-dominated systems. These $r^{1/n}$-laws, however, do not give much insight into any particular physical properties of the galaxies, such as ratios of bulge to disk radii, or bulge fraction.

Given the uncertainties in the actual profile shapes of the CL1358+62 galaxies, the fundamental plane parameter must be constructed with care. Use of the surface brightness at the half-light radius appears to be a strong function of the profile chosen for the fitting (see Figure 6). Adopting the mean surface brightness within the half-light radius produces a fundamental plane parameter which is robust against the adopted profile shape.

Although we have outlined potentially large uncertainties in half-light radii, the correlation between r and $\langle I\rangle$ ensures that the fundamental plane parameter, $r\langle I\rangle^{0.76}$ is conserved, with a scatter of 3%. In Figure 8, we show the correlation between $\langle I\rangle$ and r explicitly for the entire sample. For every trial fitting range and $r^{1/n}$-law, we plot the mean surface brightness within the fitted half-light radius, normalized by the adopted mean effective surface brightness from the de Vaucouleurs profile fit, versus galaxy radius, normalized by the effective radius from the de Vaucouleurs profile fit. The data do not deviate significantly from the correlation expected from pure $r^{1/4}$-law growth curves, shown by the dashed line. The slope running parallel to the fundamental plane, $r\langle I\rangle^{0.76}$ = constant, is shown by the solid line. Given the large uncertainties in half-light radii, the strong error correlation may not only be coincidentally parallel to the fundamental plane, but also likely seriously biases the

measured slope of the scaling relation (Kelson 1998, Kelson 1999).

Because the analysis most closely parallels earlier, ground-based work, we will use the results from the growth curve fitting in the derivation of the fundamental plane (see Kelson *et al.* 1999b).

9. CONCLUSIONS

Using deep HST imaging, we have extracted growth curves for a sample of 53 galaxies in the cluster CL1358+62 at z = 0.33. These growth curves have been fit using integrated $r^{1/4}$-laws, integrated Sersic $r^{1/n}$-law profiles, and bulge-plus-disk superpositions. Comparisons of the fits between the different parameterizations of the profiles show an *rms* scatter of 30-40% in half-light radii, although the formal uncertainties in the half-light radii from a given fit are typically smaller by factors of three. The half-light radii derived from the Sersic profiles agree in the median with those found using the $r^{1/4}$-laws at the level of 1%. The half-light radii derived using the bulge-plus-disk superpositions are systematically larger by 10%. Despite the potentially large uncertainties in the half-light radii, the quantity that enters the fundamental plane, $r_n\langle I\rangle_n^{0.76}$ has been shown to be quite stable. This combination is shown to be nearly parallel to the correlation between radius and mean surface brightness for an $r^{1/4}$-law growth curve.

The median half-light radius of this sample is $0''.61$ (2.9 kpc, $H_0 = 65\,\mathrm{km\,s^{-1}Mpc^{-1}}$, $q_0 = 0.1$), with a range of 1.26 dex in r_e. (Using B/D decompositions, or $r^{1/n}$-laws, only changes the median by $\pm 0''.01$.) The range is smaller than the 1.6 dex spanned by the Jørgensen *et al.* (1993) Coma sample, probably due to differences in selection criteria.

The median bulge fraction is about 84%. Many of the galaxies with larger bulge fractions show evidence for central exponential components in their surface brightness profiles. The few E+A galaxies in this sample invariably have disks (see also Franx *et al.* 1998. Their bulge fractions are ~65-90% (see also, *e.g.*, Wirth, Koo, & Kron 1994). Half of the sample shows evidence for disky structures after subtracting two-dimensional $r^{1/4}$-law models from the galaxy images. This result is consistent with the visual classifications in which nearly half of the sample are of type S0/a trough Sb. Two of the three E+A galaxies have evidence of spiral arms in their residual maps.

In the future, we plan to derive accurate structural parameters for the entire sample of confirmed cluster members and investigate the global correlations of these parameters with the signatures of stellar populations (color), and environment (clustercentric radius and local densities) (Tran *et al.* 2000). The importance of these issues for the fundamental plane is discussed by Kelson *et al.* (1999b). Studies of galactic structural parameters and scaling relations in distant clusters, like this program, clearly require wide-field imaging of the distant cluster fields. Two more WFPC2 mosaics have now been taken, of MS2053-04 (z = 0.58) and MS1054–03 (z = 0.83). With these clusters, the evolution of the properties of cluster galaxies can be accurately mapped to redshifts approaching unity and the Advanced Camera for Surveys is expected to extend such studies to redshifts beyond z = 1.

We gratefully acknowledge D. Koo and S. Faber, who provided valuable comments on an early version of the paper. Furthermore, we appreciate the effort of all those in the HST program that made this unique Observatory work as well as it does. The assistance of those at STScI who helped with the acquisition of the HST data is also gratefully acknowledged. Support from STScI grants GO05989.01-94A, GO05991.01-94A, and AR05798.01-94A and NSF grant AST-9529098 is gratefully acknowledged.

REFERENCES

Bender, R., *et al.* 1998, ApJ, 493, 529
Bessell, M.S. 1990, PASP, 102, 1181
Bower, R.G., Lucey, J.R., & Ellis, R.S. 1992, MNRAS, 254, 601
Burstein, D., & Heiles, C. 1982, 1982, AJ, 87, 1165
Caon, N., Capaccioli, M., & D'onofrio, M. 1993, MNRAS, 265, 1013
Cardelli, J.A., Clayton, G.C. & Mathis, J.S. 1989, ApJ, 345, 245
Djorgovski S., & Davis M. 1987, ApJ, 313, 59
Dressler, A., Lynden-Bell, D., Burstein, D., Davies, R.L., Faber, S.M, Terlevich, R.J. & Wegner, G 1987, ApJ, 313, 42
Dressler, A., Oemler, A., Jr., Couch, W. J., Smail, I., Ellis, R. S., Barger, A., Butcher, H., Poggianti, B. M., & Sharples, R. M. 1997, ApJ, 490, 577
Ellis R. S., Smail, I., Dressler, A., Couch, W.J., Oemler, A., Jr., Butcher, H., & Sharples, R.M. 1997, ApJ, 483, 582
Faber, S.M. & Jackson, R.E. 1976, ApJ, 204, 668
Faber S. M., Dressler A., Davies R. L., Burstein D., Lynden-Bell D., Terlevich R., & Wegner G. 1987, Faber S. M., ed., Nearly Normal Galaxies. Springer, New York, p. 175
Fabricant, D.G., McClintock, J.E. & Bautz, M.W. 1991, ApJ, 381, 33
Fabricant, D.G., *et al.* 1999, in preparation
Fisher, D., Fabricant, D.G., Franx, M., & van Dokkum P.G. 1998, ApJ, 498, 195
Franx M. 1993, PASP, 105, 1058
Franx M., *et al.* 1998, in preparation
Frie, Z., & Gunn, J.E. 1994, AJ, 108, 1476
Fukugita, M., Shimasaku, K., & Ichikawa T. 1995, PASP, 107, 945
Fukugita, M., Ichikawa, T., Gunn, J. E., Doi, M., Shimasaku, K., & Schneider, D. P. 1996, AJ, 111, 1748
Graham, A., & Colless, M. 1997, MNRAS, 287, 221
Hayes D.S. 1985, in Proceedings of IAU Symposium No. 111 *Calibration of Fundamental Stellar Quantities*, edited by D.S. Hayes, L.E. Pasinetti, & A.G. Davis Philip (Reidel:Dordrecht), p. 225
Hill, R.J. *et al.* 1998, ApJ, 496, 648
Högbom J. A. 1974, A&AS, 15, 417
Holtzman, J. A., Burrows, C. J., Casertano, S., Hester, J. J., Trauger, J. T., Watson, A. M., & Worthey, G. 1995, PASP, 107, 1065
Hook, R.N. & Fruchter, A.S. 1997 Astronomical Data Analysis Software and Systems VI, ASP Conference Series, Vol. 125, G. Hunt, H.E. Payne, eds., p. 147
Jørgensen I., Franx M., & Kjærgaard P. 1992, A&AS, 95, 489
Jørgensen I., Franx M., & Kjærgaard P. 1993, ApJ, 411, 34
Jørgensen I., Franx M., & Kjærgaard P. 1996, MNRAS, 280, 167
Kelson, D.D. 1998, Ph.D. thesis, Univ. of California, Santa Cruz
Kelson, D.D., van Dokkum, P.G., Franx, M., Illingworth, G.D., & Fabricant, D.G. 1997, ApJL, 478, L13
Kelson, D.D. *et al.* 1999a, ApJ, submitted
Kelson, D.D. *et al.* 1999b, ApJ, submitted
Kelson, D.D. 1999, ApJ, *in preparation*
Kelson, D.D. *et al.* 1999, ApJ, *in preparation*
Kormendy, J. 1977, ApJ, 218, 333
Krist J. 1995, Astronomical Data Analysis Software and Systems IV, ASP Conference Series, Vol. 77, R.A. Shaw, H.E. Payne, and J.J.E. Hayes, eds., p. 349.
Krist J., & Hook, R. 1997, The Tiny Tim User's Manual, version 4.3.
Lucey, J.R., Bower, R.G., & Ellis, R.S. 1991, MNRAS, 249, 755
Oemler, A., Jr. 1974, ApJ, 194, 10
Oke, J.B., & Gunn, J.E. 1983, ApJ, 266, 713
Oke, J.B., *et al.* 1995, PASP, 107, 375
Pahre, M. A., Djorgovski, S. G., & de Carvalho, R. R. 1995, ApJL, 453, L17
Pahre, M. A., Djorgovski, S. G., & de Carvalho, R. R. 1998, AJ, *submitted*
Pence W. 1976, ApJ, 203, 39
Phillips, A.C. *et al.* 1995, ApJ, 444, 21
Saglia, R.P., *et al.* 1993, MNRAS, 264, 961
Saglia, R.P., *et al.* 1997, ApJS, 109, 79
Schade, D., Carlberg, R.G., Yee, H.K.C & López-Cruz, O. 1997, ApJL, 477, L17
Sersic, J.L. 1968, *Atlas de Galaxia Australes*, (Cordoba: Observatorio Astronomico)
Simard, L. 1998, ASP Conf. Ser. 145: Astronomical Data Analysis Software and Systems VII, R. Albrecht, R.N. Hook and H.A. Bushouse, eds. 7, 108
Simard, L., *et al.* 1999, ApJ, in press

Stetson, P.B. 1998, PASP, 110,1448
Stetson, P.B. *et al.* 1998, ApJ, 508, 491
Tran, K.-V., *et al.* 2000, ApJ, *in preparation*
Tully, R.B. & Fisher J.R. 1977, A&A, 54, 661
van Dokkum, P. G., & Franx M. 1996, MNRAS, 281, 985
van Dokkum, P.G., Franx, M., Illingworth, G. D., Kelson, D. D., Fisher, D., & Fabricant, D. 1998a, ApJ, 500, 714
van Dokkum, P. G., Franx, M., Kelson, D. D., & Illingworth, G. D. 1998b, ApJ, 504, L17
Vogt, N. P., Forbes, D. A., Phillips, A. C., Gronwall, C., Faber, S. M., Illingworth, G. D., & Koo, D. C. 1996, ApJL, 465, L15
Vogt, N. P., Phillips, A. C., Faber, S. M., Gallego, J., Gronwall, C., Guzmán, R., Illingworth, G. D., Koo, D. C., & Lowenthal, J.D. 1997, ApJL, 479, L121
Wirth, G.D., Koo, D.C., & Kron, R.G. 1994, ApJL, 435, L105
Ziegler, B. L., & Bender, R. 1997, MNRAS, 291, 527

TABLE 1
1D $r^{1/4}$- AND $r^{1/n}$-LAW STRUCTURAL PARAMETERS

			$r^{1/4}$-law			$r^{1/n}$-law			
ID (1)	Type (2)	$(B-V)_z$	r_e (4)	$\langle\mu\rangle_e$ (5)	$r_e\langle I\rangle_e^{0.76}$ (6)	n (7)	r_n (8)	$\langle\mu\rangle_n$ (9)	$r_n\langle I\rangle_n^{0.76}$ (10)
095	S0	0.894	0.356	19.84	2.59	5.2	0.565	20.59	2.56
...	...	...	±0.004	±0.02	...	±1.2	±0.005	±0.02	...
110	S0/a	0.850	0.648	20.32	2.70	2.3	0.375	19.53	2.71
...	...	...	±0.012	±0.04	...	±0.4	±0.005	±0.03	...
129	S0/a	0.830	0.324	19.27	2.72	4.2	0.326	19.28	2.72
...	...	...	±0.004	±0.02	...	±0.3	±0.004	±0.03	...
135	S0	0.827	0.351	20.19	2.48	5.2	0.493	20.71	2.47
...	...	...	±0.009	±0.05	...	±0.3	±0.010	±0.04	...
142	S0/a	0.856	1.414	22.15	2.49	3.9	1.398	22.13	2.49
...	...	...	±0.046	±0.07	...	±0.9	±0.046	±0.07	...
164	S0/a	0.870	1.165	21.56	2.58	5.7	1.955	22.37	2.56
...	...	...	±0.035	±0.06	...	±0.7	±0.100	±0.08	...
182	S0	0.839	0.418	20.70	2.40	3.2	0.310	20.25	2.40
...	...	...	±0.008	±0.04	...	±0.3	±0.005	±0.04	...
209	Sa	0.601	0.980	21.34	2.57	2.3	0.557	20.49	2.59
...	...	...	±0.018	±0.04	...	±0.3	±0.005	±0.02	...
211	S0	0.870	0.612	20.58	2.60	3.3	0.470	20.18	2.61
...	...	...	±0.015	±0.05	...	±0.4	±0.009	±0.04	...
212	E	0.868	0.547	20.44	2.59	5.2	0.781	21.01	2.58
...	...	...	±0.009	±0.03	...	±0.3	±0.008	±0.02	...
215	S0	0.843	0.338	20.17	2.47	5.0	0.460	20.67	2.45
...	...	...	±0.006	±0.03	...	±1.0	±0.007	±0.03	...
233	E/S0	0.847	0.590	19.95	2.78	5.3	0.873	20.58	2.75
...	...	...	±0.012	±0.04	...	±0.4	±0.010	±0.03	...
234	Sb	0.689	3.636	23.68	2.43	3.0	2.264	22.97	2.44
...	...	...	±0.349	±0.18	...	±1.0	±0.166	±0.16	...
236	S0	0.895	0.539	20.51	2.57	5.5	0.892	21.33	2.53
...	...	...	±0.009	±0.03	...	±1.5	±0.010	±0.03	...
242	E	0.882	1.201	21.54	2.60	4.2	1.210	21.55	2.60
...	...	...	±0.026	±0.04	...	±0.3	±0.026	±0.04	...
256	E	0.875	0.956	20.30	2.88	5.4	1.542	21.06	2.86
...	...	...	±0.010	±0.02	...	±0.4	±0.010	±0.02	...
269	E/S0	0.913	0.776	20.05	2.86	5.0	1.056	20.55	2.85
...	...	...	±0.008	±0.02	...	±1.0	±0.008	±0.01	...
292	S0/a	0.776	0.911	21.21	2.58	2.4	0.562	20.50	2.59
...	...	...	±0.031	±0.07	...	±0.5	±0.009	±0.04	...
298	S0	0.914	0.642	19.93	2.82	2.5	0.406	19.23	2.83
...	...	...	±0.007	±0.02	...	±0.5	±0.002	±0.01	...
300	S0	0.879	0.386	19.59	2.70	3.4	0.310	19.25	2.71
...	...	...	±0.004	±0.02	...	±0.4	±0.002	±0.02	...
303	E	0.858	0.494	20.18	2.63	5.3	0.729	20.81	2.61
...	...	...	±0.007	±0.03	...	±0.4	±0.007	±0.02	...
309	E/S0	0.900	0.433	19.80	2.69	4.9	0.572	20.23	2.68
...	...	...	±0.003	±0.01	...	±1.0	±0.003	±0.01	...
328	Sa	0.629	0.878	21.15	2.58	2.5	0.550	20.45	2.59
...	...	...	±0.016	±0.04	...	±0.6	±0.008	±0.02	...
335	S0/a	0.859	0.512	20.79	2.46	4.4	0.551	20.89	2.46
...	...	...	±0.009	±0.04	...	±0.4	±0.009	±0.04	...
343	S0	0.670	0.438	20.66	2.43	3.3	0.353	20.33	2.44
...	...	...	±0.010	±0.05	...	±0.4	±0.007	±0.05	...
353	E/S0	0.889	0.958	20.79	2.73	5.4	1.495	21.52	2.70
...	...	...	±0.007	±0.01	...	±0.5	±0.008	±0.01	...
356	Sa	0.889	0.815	20.62	2.71	3.9	0.741	20.48	2.71
...	...	...	±0.011	±0.03	...	±0.2	±0.011	±0.02	...
359	S0	0.851	0.475	19.95	2.68	4.4	0.527	20.12	2.68
...	...	...	±0.005	±0.02	...	±0.4	±0.005	±0.02	...
360	E	0.861	0.241	19.65	2.48	5.5	0.373	20.37	2.45
...	...	...	±0.004	±0.03	...	±0.6	±0.009	±0.04	...
366	S0/a	0.863	0.587	20.68	2.55	3.3	0.448	20.28	2.56
...	...	...	±0.008	±0.03	...	±0.4	±0.005	±0.03	...
368	Sab	0.862	1.055	22.09	2.38	2.4	0.649	21.34	2.39
...	...	...	±0.032	±0.06	...	±2.6	±0.010	±0.04	...
369	S0/a	0.879	0.935	21.70	2.44	4.3	0.985	21.78	2.44
...	...	...	±0.023	±0.05	...	±0.4	±0.023	±0.05	...
371	Sa	0.871	1.699	21.84	2.66	3.5	1.456	21.61	2.66
...	...	...	±0.033	±0.04	...	±1.5	±0.018	±0.03	...
372	Sa	0.867	1.595	22.09	2.56	3.2	1.191	21.64	2.57
...	...	...	±0.064	±0.08	...	±1.2	±0.034	±0.06	...
375	E	0.894	3.813	22.44	2.83	6.0	7.498	23.53	2.79
...	...	...	±0.075	±0.04	...	±0.2	±0.231	±0.06	...
381	E/S0	0.866	0.392	19.92	2.61	6.0	0.756	20.97	2.57
...	...	...	±0.008	±0.04	...	±0.2	±0.020	±0.05	...
397	S0/a	0.851	0.727	21.29	2.46	3.3	0.472	20.71	2.45
...	...	...	±0.020	±0.06	...	±0.4	±0.011	±0.04	...
408	S0	0.861	0.353	19.70	2.63	3.4	0.291	19.41	2.63
...	...	...	±0.003	±0.02	...	±0.5	±0.002	±0.02	...
409	E	0.895	0.536	21.38	2.30	4.1	0.525	21.35	2.30
...	...	...	±0.005	±0.02	...	±1.1	±0.005	±0.02	...
410	S0	0.870	0.497	20.70	2.47	3.2	0.370	20.26	2.48
...	...	...	±0.008	±0.03	...	±0.3	±0.005	±0.03	...
412	E	0.843	0.368	20.22	2.49	6.0	0.795	21.44	2.45
...	...	...	±0.007	±0.04	...	±0.2	±0.023	±0.06	...
433	S0/a	0.851	0.371	19.95	2.57	6.0	0.907	21.42	2.51
...	...	...	±0.011	±0.06	...	±0.2	±0.039	±0.09	...
440	S0/a	0.843	0.663	21.67	2.30	4.9	0.843	22.02	2.30
...	...	...	±0.016	±0.05	...	±0.9	±0.020	±0.04	...
454	S0/a	0.807	0.983	21.16	2.63	2.3	0.613	20.46	2.64
...	...	...	±0.014	±0.03	...	±0.3	±0.005	±0.02	...
463	S0	0.883	0.667	20.50	2.66	3.2	0.492	20.03	2.67
...	...	...	±0.007	±0.02	...	±0.3	±0.004	±0.02	...
465	Sa	0.873	0.581	20.93	2.47	4.2	0.599	20.98	2.47
...	...	...	±0.009	±0.03	...	±0.3	±0.009	±0.03	...
481	S0	0.810	0.478	21.06	2.35	2.3	0.334	20.54	2.35
...	...	...	±0.015	±0.06	...	±0.4	±0.005	±0.03	...
493	E/S0	0.809	0.207	20.09	2.28	4.1	0.214	20.15	2.27
...	...	...	±0.010	±0.10	...	±1.1	±0.010	±0.10	...
523	S0/a	0.905	0.910	21.42	2.52	4.0	0.863	21.34	2.52
...	...	...	±0.016	±0.04	...	±1.0	±0.016	±0.03	...
531	E	0.887	1.048	20.63	2.82	5.4	1.682	21.39	2.79
...	...	...	±0.009	±0.02	...	±0.4	±0.010	±0.01	...
534	E	0.888	0.464	20.77	2.42	4.4	0.486	20.84	2.42
...	...	...	±0.008	±0.04	...	±0.4	±0.008	±0.04	...
536	E	0.874	0.890	20.63	2.75	5.2	1.355	21.29	2.73
...	...	...	±0.009	±0.02	...	±0.3	±0.010	±0.02	...
549	Sab	0.760	1.592	22.77	2.35	3.5	1.380	22.54	2.36
...	...	...	±0.058	±0.07	...	±0.5	±0.033	±0.06	...

NOTE.— Morphological types taken from Fabricant *et al.* (1999); restframe $(B-V)_z$ colors taken from van Dokkum *et al.* (1998a); radii expressed in arcsec and surface brightnesses in mag per square arcsec, except for the fundamental plane parameters in which the radii have been transformed to kpc and the surface brightnesses to $L_\odot/\mathrm{pc}^2$; these structural parameters were derived by fitting the integrated profiles between $r = 0''.1$ and $r \approx 2\,r_{1/2}$.

TABLE 2
1D BULGE-DISK DECOMPOSITIONS

ID	Type	Total			Bulge		Disk		Bulge Fraction			Total	ϵ
		$r_{1/2}$	$\langle\mu\rangle_{1/2}$	$r_{1/2}\langle I\rangle_{1/2}^{0.76}$	$r_{1/2}$	$\langle\mu\rangle_{1/2}$	$r_{1/2}$	$\langle\mu\rangle_{1/2}$	$\leq 0''.2$	$\leq 0''.5$	$\leq 2r_{1/2}$		
(1)	(2)	(3)	(4)	(5)	(6)	(7)	(8)	(9)	(10)	(11)	(12)	(13)	(14)
095	S0	0.704	20.94	2.55	0.986	21.84	0.064	17.75	0.46	0.64	0.77	0.85	0.15
...		±0.056	±0.48	...	±0.078	±0.15	±0.005	±0.12	±0.04	±0.02	±0.01	±0.01	...
110	S0/a	0.350	19.45	2.70	0.102	18.36	0.419	20.12	0.51	0.31	0.26	0.23	0.69
...		±0.059	±0.91	...	±0.063	±0.95	±0.014	±0.16	±0.02	±0.03	±0.04	±0.02	...
129	S0/a	0.489	19.93	2.70	0.726	20.95	0.047	16.68	0.48	0.65	0.73	0.82	0.27
...		±0.035	±0.42	...	±0.059	±0.14	±0.001	±0.03	±0.02	±0.01	±0.01	±0.01	...
135	S0	0.418	20.45	2.47	0.490	20.87	0.039	18.01	0.76	0.85	0.88	0.92	0.43
...		±0.046	±0.69	...	±0.048	±0.20	±0.009	±0.37	±0.05	±0.03	±0.02	±0.01	...
142	S0/a	0.834	21.40	2.48	0.318	20.47	1.094	22.44	0.84	0.64	0.39	0.34	0.36
...		±0.150	±0.85	...	±0.127	±0.55	±0.072	±0.25	±0.01	±0.01	±0.02	±0.02	...
164	S0/a	2.251	22.62	2.54	2.541	22.92	0.061	17.77	0.46	0.68	0.91	0.94	0.12
...		±0.188	±0.45	...	±0.207	±0.13	±0.007	±0.19	±0.06	±0.03	±0.00	±0.01	...
182	S0	0.355	20.46	2.40	0.392	20.77	0.220	21.91	0.87	0.85	0.86	0.90	0.43
...		±0.024	±0.34	...	±0.023	±0.10	±0.034	±0.30	±0.02	±0.02	±0.02	±0.02	...
209	Sa	0.625	20.65	2.59	0.960	22.06	0.427	20.93	0.59	0.50	0.52	0.64	0.69
...		±0.085	±0.60	...	±0.166	±0.24	±0.030	±0.11	±0.01	±0.01	±0.01	±0.01	...
211	S0	0.448	20.12	2.61	0.458	20.41	0.432	21.68	0.85	0.77	0.74	0.78	0.61
...		±0.051	±0.46	...	±0.051	±0.15	±0.052	±0.18	±0.01	±0.02	±0.03	±0.02	...
212	E	0.683	20.78	2.59	0.781	21.17	0.052	18.03	0.70	0.83	0.89	0.93	0.09
...		±0.036	±0.32	...	±0.034	±0.09	±0.009	±0.27	±0.04	±0.02	±0.01	±0.01	...
215	S0	0.457	20.66	2.45	0.700	21.77	0.037	16.95	0.47	0.64	0.71	0.81	0.29
...		±0.036	±0.46	...	±0.056	±0.15	±0.003	±0.13	±0.03	±0.01	±0.01	±0.01	...
233	E/S0	0.784	20.40	2.76	0.952	20.94	0.113	18.74	0.64	0.76	0.86	0.90	0.35
...		±0.086	±0.76	...	±0.104	±0.23	±0.014	±0.17	±0.08	±0.05	±0.03	±0.01	...
234	Sb	0.996	21.86	2.42	0.035	17.80	1.049	22.03	0.55	0.22	0.06	0.05	0.40
...		±0.113	±0.51	...	±0.041	±2.22	±0.058	±0.10	±0.01	±0.01	±0.01	±0.02	...
236	S0	0.776	21.10	2.55	0.944	21.63	0.055	17.87	0.59	0.75	0.86	0.90	0.29
...		±0.047	±0.37	...	±0.055	±0.11	±0.004	±0.12	±0.04	±0.02	±0.01	±0.01	...
242	E	1.529	21.92	2.59	1.825	22.42	0.263	20.72	0.69	0.70	0.87	0.91	0.10
...		±0.171	±0.76	...	±0.214	±0.22	±0.015	±0.24	±0.07	±0.06	±0.02	±0.02	...
256	E	1.380	20.88	2.86	1.551	21.20	0.090	18.00	0.63	0.78	0.91	0.94	0.14
...		±0.073	±0.33	...	±0.071	±0.09	±0.014	±0.25	±0.05	±0.03	±0.01	±0.01	...
269	E/S0	0.962	20.39	2.85	1.045	20.62	0.093	18.71	0.78	0.87	0.94	0.96	0.35
...		±0.058	±0.39	...	±0.056	±0.11	±0.019	±0.28	±0.05	±0.03	±0.01	±0.01	...
292	S0/a	0.486	20.32	2.58	0.297	20.39	0.561	21.10	0.64	0.44	0.36	0.35	0.26
...		±0.137	±1.35	...	±0.218	±0.93	±0.022	±0.26	±0.02	±0.03	±0.04	±0.01	...
298	S0	0.554	19.69	2.83	0.835	20.84	0.240	19.53	0.61	0.60	0.68	0.78	0.67
...		±0.052	±0.56	...	±0.088	±0.19	±0.013	±0.14	±0.03	±0.02	±0.01	±0.01	...
300	S0	0.453	19.84	2.69	0.584	20.53	0.092	18.66	0.66	0.77	0.82	0.88	0.41
...		±0.028	±0.43	...	±0.039	±0.13	±0.002	±0.10	±0.03	±0.02	±0.01	±0.01	...
303	E	0.638	20.59	2.61	0.774	21.11	0.091	18.89	0.67	0.78	0.86	0.90	0.15
...		±0.058	±0.63	...	±0.068	±0.19	±0.012	±0.16	±0.06	±0.04	±0.03	±0.01	...
309	E/S0	0.502	20.02	2.68	0.540	20.21	0.060	18.91	0.87	0.92	0.94	0.96	0.14
...		±0.023	±0.31	...	±0.020	±0.08	±0.016	±0.40	±0.04	±0.02	±0.02	±0.01	...
328	Sa	0.666	20.72	2.59	0.862	21.53	0.392	21.30	0.76	0.69	0.71	0.80	0.47
...		±0.082	±0.58	...	±0.108	±0.19	±0.046	±0.20	±0.02	±0.02	±0.02	±0.01	...
335	S0/a	0.539	20.86	2.46	0.541	20.90	0.059	20.61	0.94	0.97	0.98	0.99	0.37
...		±0.040	±0.51	...	±0.033	±0.14	±0.053	±1.28	±0.06	±0.04	±0.02	±0.01	...
343	S0	0.404	20.54	2.43	0.492	21.10	0.165	20.93	0.77	0.80	0.83	0.88	0.44
...		±0.038	±0.54	...	±0.045	±0.16	±0.020	±0.30	±0.03	±0.02	±0.02	±0.02	...
353	E/S0	1.120	21.05	2.72	1.205	21.24	0.134	19.97	0.81	0.88	0.94	0.96	0.02
...		±0.051	±0.32	...	±0.050	±0.09	±0.021	±0.22	±0.04	±0.03	±0.01	±0.01	...
356	Sa	0.604	20.20	2.71	0.392	19.78	0.899	22.07	0.90	0.79	0.65	0.61	0.46
...		±0.044	±0.31	...	±0.035	±0.11	±0.039	±0.17	±0.00	±0.00	±0.01	±0.02	...
359	S0	0.574	20.26	2.67	0.769	21.05	0.122	19.05	0.61	0.71	0.79	0.86	0.20
...		±0.056	±0.71	...	±0.082	±0.22	±0.005	±0.13	±0.06	±0.04	±0.03	±0.01	...
360	E	0.341	20.22	2.45	0.594	21.66	0.050	17.62	0.45	0.61	0.65	0.77	0.31
...		±0.056	±1.00	...	±0.103	±0.34	±0.007	±0.21	±0.05	±0.03	±0.02	±0.01	...
366	S0/a	0.630	20.79	2.55	0.718	21.16	0.140	20.46	0.80	0.85	0.90	0.93	0.28
...		±0.038	±0.44	...	±0.044	±0.12	±0.008	±0.25	±0.04	±0.03	±0.02	±0.01	...
368	Sab	0.542	21.10	2.39	0.627	22.39	0.514	21.56	0.53	0.39	0.34	0.41	0.63
...		±0.139	±0.97	...	±0.317	±0.62	±0.043	±0.10	±0.01	±0.01	±0.02	±0.02	...
369	S0/a	1.036	21.86	2.44	1.085	21.98	0.079	20.28	0.85	0.92	0.96	0.98	0.30
...		±0.077	±0.48	...	±0.075	±0.13	±0.024	±0.41	±0.06	±0.03	±0.01	±0.01	...
371	Sa	0.956	21.04	2.66	0.468	20.64	1.169	21.92	0.81	0.63	0.37	0.34	0.54
...		±0.118	±0.61	...	±0.147	±0.42	±0.029	±0.14	±0.00	±0.01	±0.02	±0.01	...
372	Sa	1.435	21.92	2.56	1.905	22.72	0.593	21.99	0.78	0.71	0.77	0.84	0.77
...		±0.211	±0.79	...	±0.280	±0.24	±0.088	±0.32	±0.03	±0.05	±0.03	±0.02	...
375	E	4.979	22.86	2.82	5.267	23.01	0.162	19.22	0.54	0.69	0.96	0.97	0.05
...		±0.313	±0.37	...	±0.295	±0.10	±0.046	±0.47	±0.13	±0.07	±0.01	±0.01	...
381	E/S0	0.512	20.34	2.60	0.550	20.50	0.088	20.02	0.88	0.92	0.94	0.96	0.37
...		±0.063	±0.89	...	±0.060	±0.25	±0.041	±0.64	±0.10	±0.07	±0.05	±0.02	...
397	S0/a	0.409	20.50	2.45	0.111	18.96	0.540	21.45	0.68	0.44	0.35	0.29	0.57
...		±0.035	±0.45	...	±0.026	±0.36	±0.014	±0.10	±0.01	±0.01	±0.01	±0.01	...
408	S0	0.382	19.82	2.63	0.523	20.66	0.096	18.86	0.63	0.74	0.77	0.85	0.54
...		±0.020	±0.37	...	±0.030	±0.12	±0.002	±0.08	±0.02	±0.01	±0.01	±0.01	...
409	E	0.498	21.27	2.30	0.542	21.49	0.223	22.60	0.90	0.90	0.92	0.94	0.10
...		±0.028	±0.41	...	±0.026	±0.11	±0.041	±0.62	±0.04	±0.03	±0.02	±0.02	...
410	S0	0.488	20.67	2.47	0.575	21.13	0.157	20.84	0.80	0.83	0.87	0.91	0.43
...		±0.032	±0.46	...	±0.037	±0.13	±0.013	±0.29	±0.04	±0.03	±0.02	±0.02	...
412	E	0.767	21.39	2.45	1.091	22.32	0.056	17.66	0.42	0.61	0.76	0.84	0.32
...		±0.072	±0.56	...	±0.096	±0.17	±0.007	±0.22	±0.06	±0.03	±0.01	±0.01	...
433	S0/a	1.021	21.61	2.51	1.397	22.46	0.072	17.95	0.40	0.59	0.78	0.85	0.11
...		±0.189	±1.10	...	±0.251	±0.34	±0.016	±0.36	±0.11	±0.06	±0.03	±0.01	...
440	S0/a	1.108	22.45	2.29	1.328	22.98	0.061	18.80	0.54	0.72	0.87	0.91	0.34
...		±0.109	±0.58	...	±0.128	±0.17	±0.007	±0.17	±0.06	±0.03	±0.01	±0.01	...
454	S0/a	0.595	20.42	2.64	0.990	22.27	0.461	20.61	0.47	0.37	0.37	0.50	0.58
...		±0.068	±0.50	...	±0.182	±0.26	±0.020	±0.07	±0.00	±0.00	±0.00	±0.01	...
463	S0	0.639	20.43	2.66	0.714	20.74	0.229	21.18	0.87	0.87	0.91	0.94	0.48
...		±0.044	±0.46	...	±0.046	±0.13	±0.033	±0.46	±0.04	±0.03	±0.02	±0.02	...
465	Sa	0.609	21.01	2.47	0.660	21.22	0.133	21.10	0.87	0.90	0.94	0.96	0.48
...		±0.050	±0.64	...	±0.053	±0.18	±0.019	±0.59	±0.07	±0.05	±0.03	±0.02	...
481	S0	0.260	20.25	2.33	0.157	20.76	0.280	20.65	0.32	0.22	0.22	0.22	0.74
...		±0.036	±0.65	...	±0.090	±0.70	±0.004	±0.12	±0.03	±0.04	±0.04	±0.02	...
493	E/S0	0.193	19.98	2.28	0.374	21.66	0.059	18.74	0.48	0.61	0.58	0.73	0.44
...		±0.049	±1.85	...	±0.119	±0.68	±0.005	±0.17	±0.08	±0.05	±0.05	±0.01	...
523	S0/a	1.044	21.64	2.51	1.171	21.96	0.197	21.08	0.80	0.83	0.91	0.94	0.25
...		±0.079	±0.52	...	±0.089	±0.15	±0.013	±0.30	±0.05	±0.04	±0.02	±0.02	...
531	E	1.549	21.26	2.80	1.830	21.71	0.182	19.30	0.61	0.69	0.88	0.92	0.25
...		±0.088	±0.39	...	±0.102	±0.11	±0.013	±0.10	±0.04	±0.04	±0.01	±0.01	...
534	E	0.620	21.21	2.41	0.878	22.17	0.032	16.68	0.44	0.63	0.74	0.83	0.24
...		±0.043	±0.38	...	±0.060	±0.12	±0.003	±0.15	±0.02	±0.01	±0.01	±0.01	...
536	E	1.266	21.18	2.73	1.433	21.52	0.096	18.57	0.64	0.78	0.91	0.94	0.27
...		±0.063	±0.31	...	±0.064	±0.09	±0.012	±0.19	±0.04	±0.03	±0.01	±0.01	...
549	Sab	0.866	21.92	2.34	0.142	19.90	1.028	22.50	0.74	0.47	0.21	0.17	0.16
...		±0.120	±0.70	...	±0.080	±0.92	±0.049	±0.15	±0.01	±0.02	±0.03	±0.01	...

NOTE.— Morphological types taken from Fabricant *et al.* (1999); restframe $(B-V)_z$ colors taken from van Dokkum *et al.* (1998a); radii expressed in arcsec and surface brightnesses in mag per square arcsec, except for the fundamental plane parameters in which the radii have been transformed to kpc and the surface brightnesses to $L_\odot/\mathrm{pc}^2$; these structural parameters were derived by fitting the integrated profiles between $r = 0''.1$ and $r \approx 2\,r_{1/2}$. Apparent ellipticities derived from direct image fitting and are luminosity-weighted mean values for ϵ.

FIG. 1.— Color images of the fundamental plane sample of CL1358+62 galaxies generated from the F606W and F814W HST imaging. The boxes are 15″ on each side. The galaxies classified as E+A are ID # 209, 328, and 343. Galaxy # 234 is a star-forming emission line galaxy. Galaxy # 375 is the BCG.

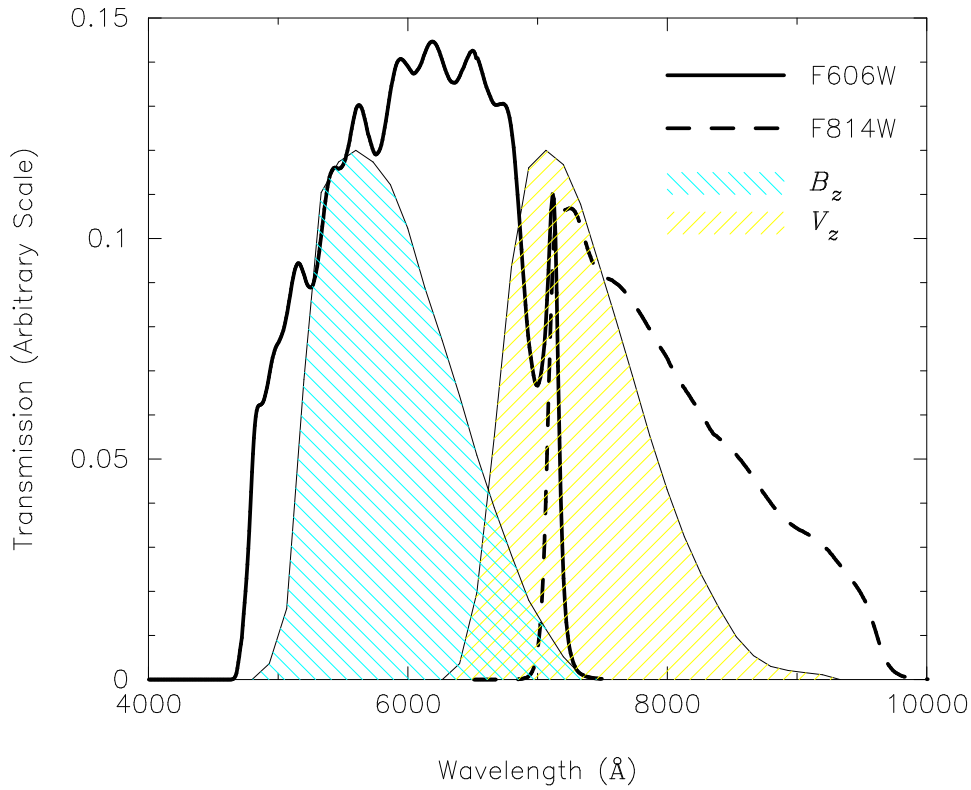

FIG. 2.— The transmission curves for the WFPC2 filters F606W and F814W are superimposed with the Johnson B_z and V_z transmission curves redshifted to $z = 0.33$.

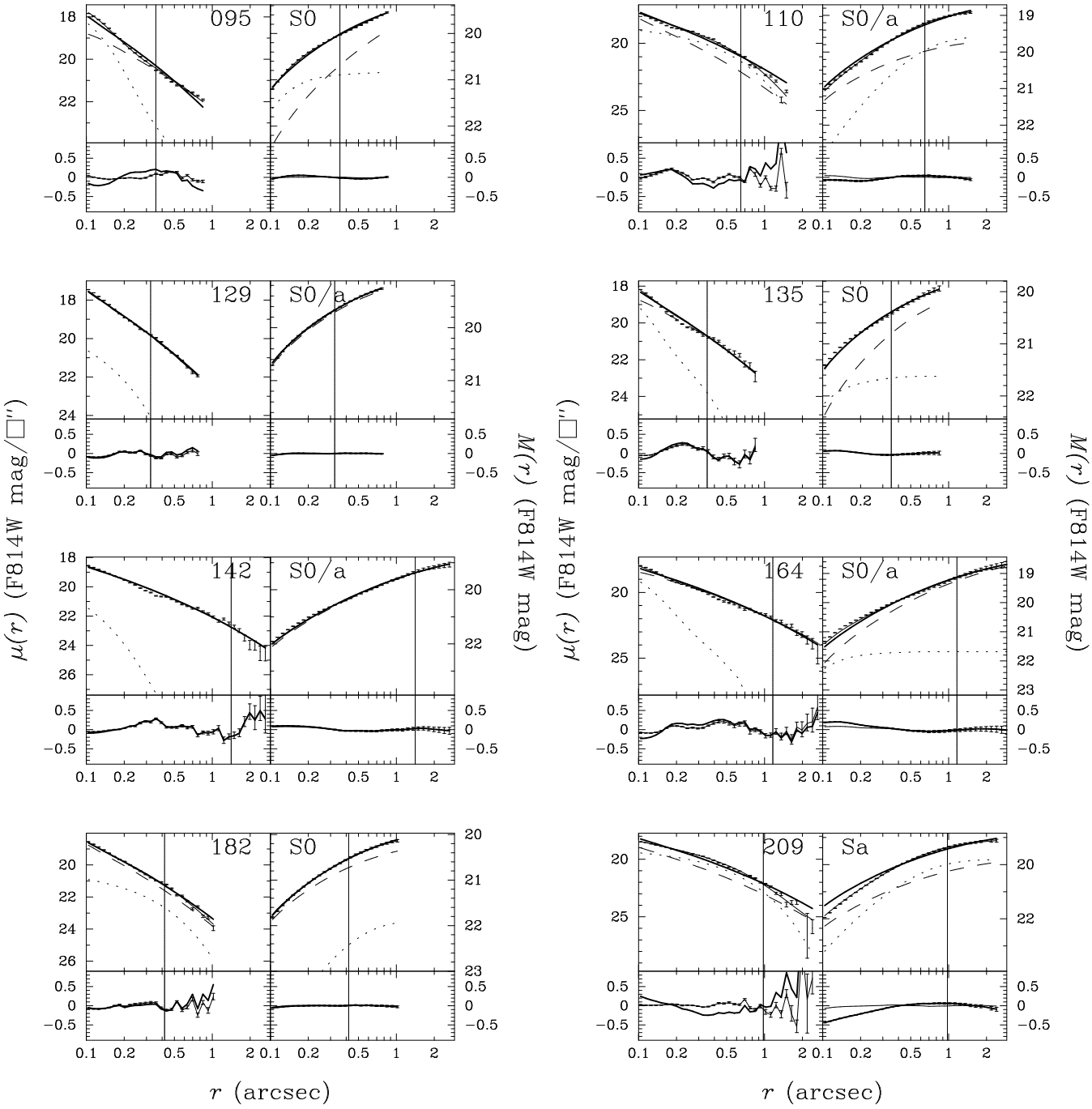

FIG. 3.— The F814W surface brightness profiles and integrated profiles from r = 1 pixel to ~$2r_e$. The thick solid lines show the fit of, and residuals from, the fit of the $r^{1/4}$-law. The thin solid lines show the fit of and residuals from the bulge-plus-disk superposition, with the two components of the fit shown as dashed ($r^{1/4}$-law bulge) and dotted (exponential disk) lines. The integrated curves were fit between r = 1 pixel and $2r_{1/2}$. Several galaxies are not well fit by a pure de Vaucouleurs profile, though as noted in the text, the effect of such deviations on the determinations of the fundamental plane parameter, $r_e\langle I\rangle_e^{0.76}$, is quite small. The profiles and growth curves are plotted over a range of $0''.1 \leq r \leq 5''$, except for galaxies # 353, 371, and 375.

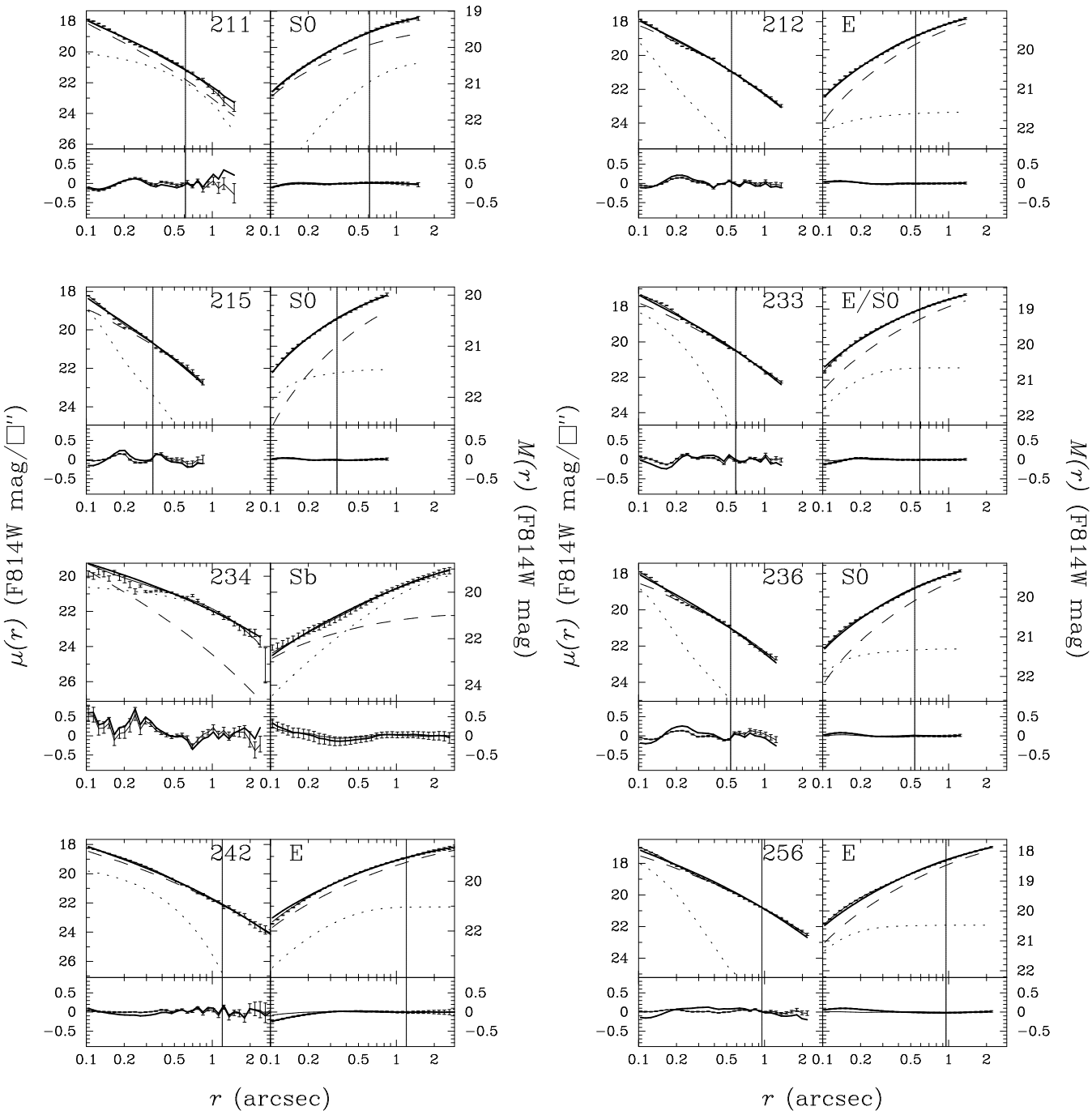

FIG. 3. (continued) —

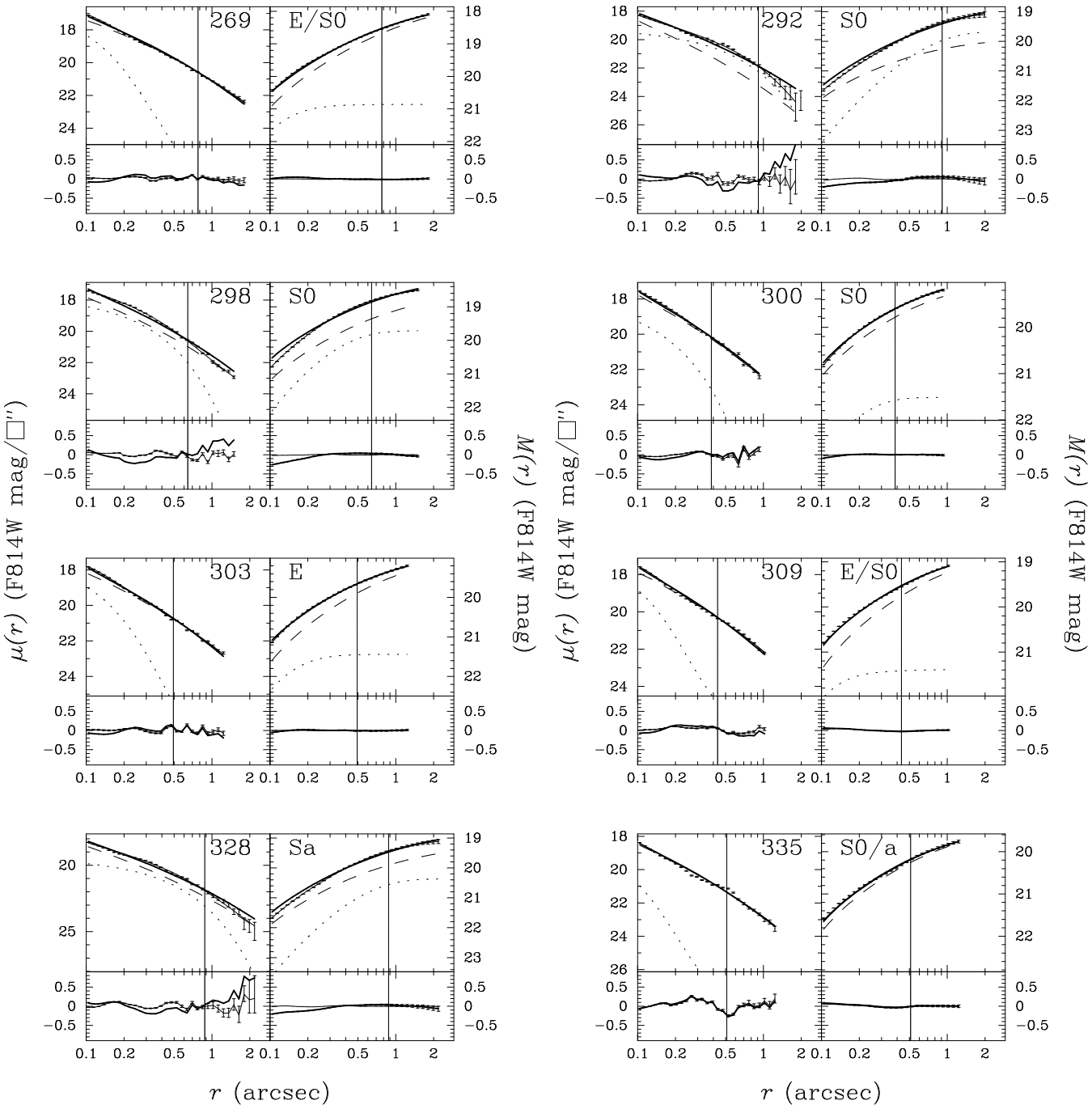

FIG. 3. (continued) —

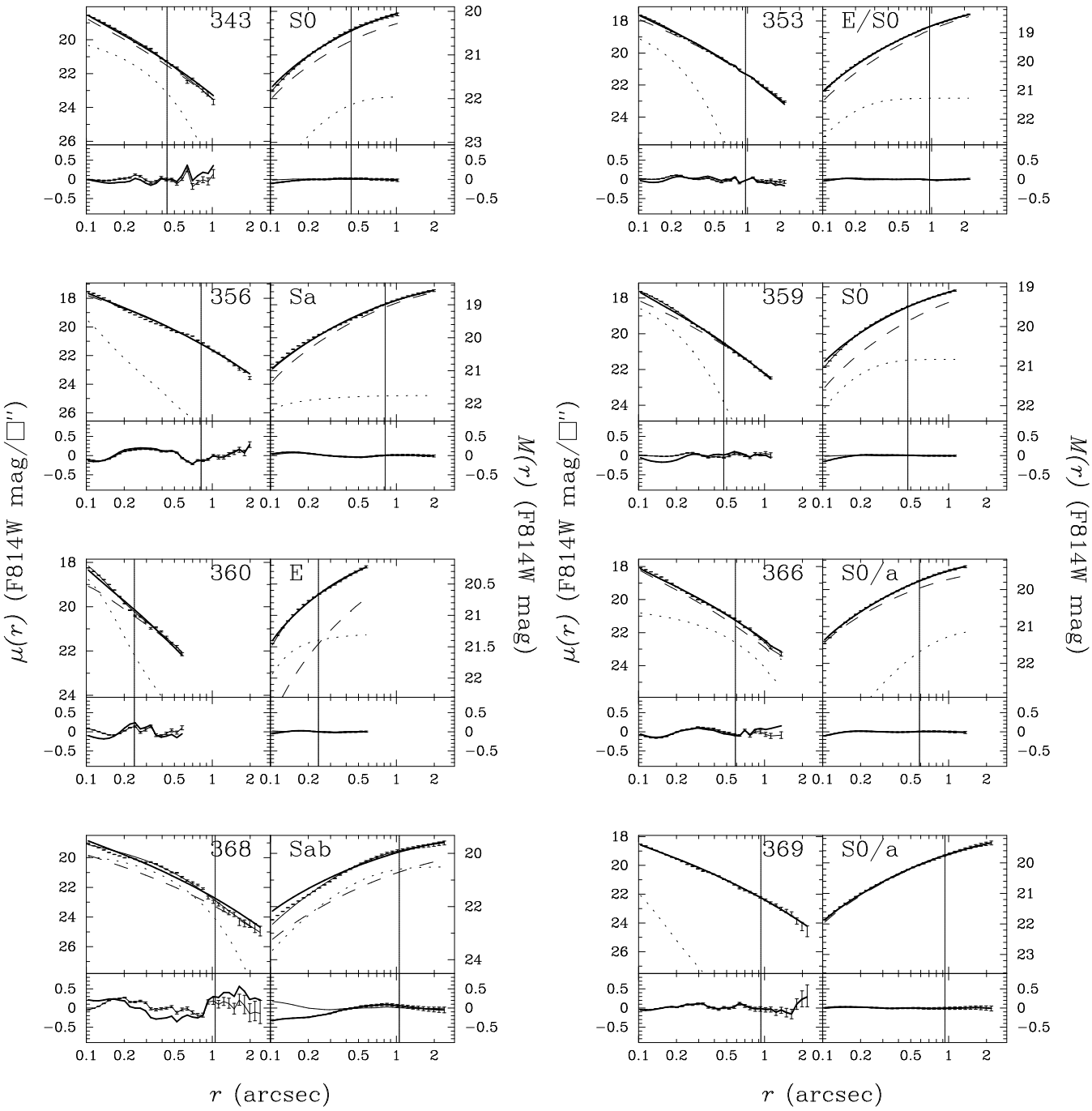

FIG. 3. (continued) —

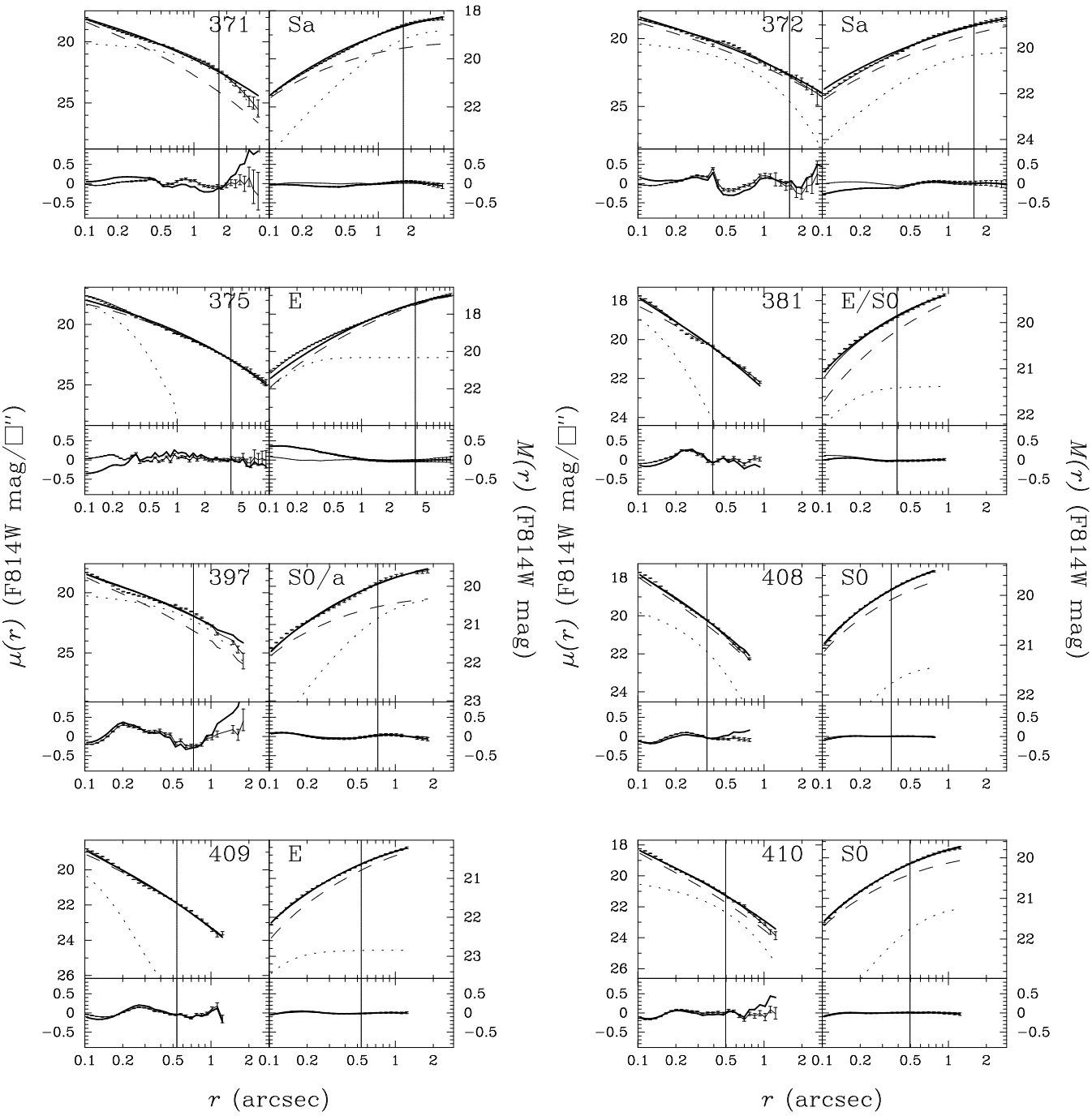

FIG. 3. (continued) —

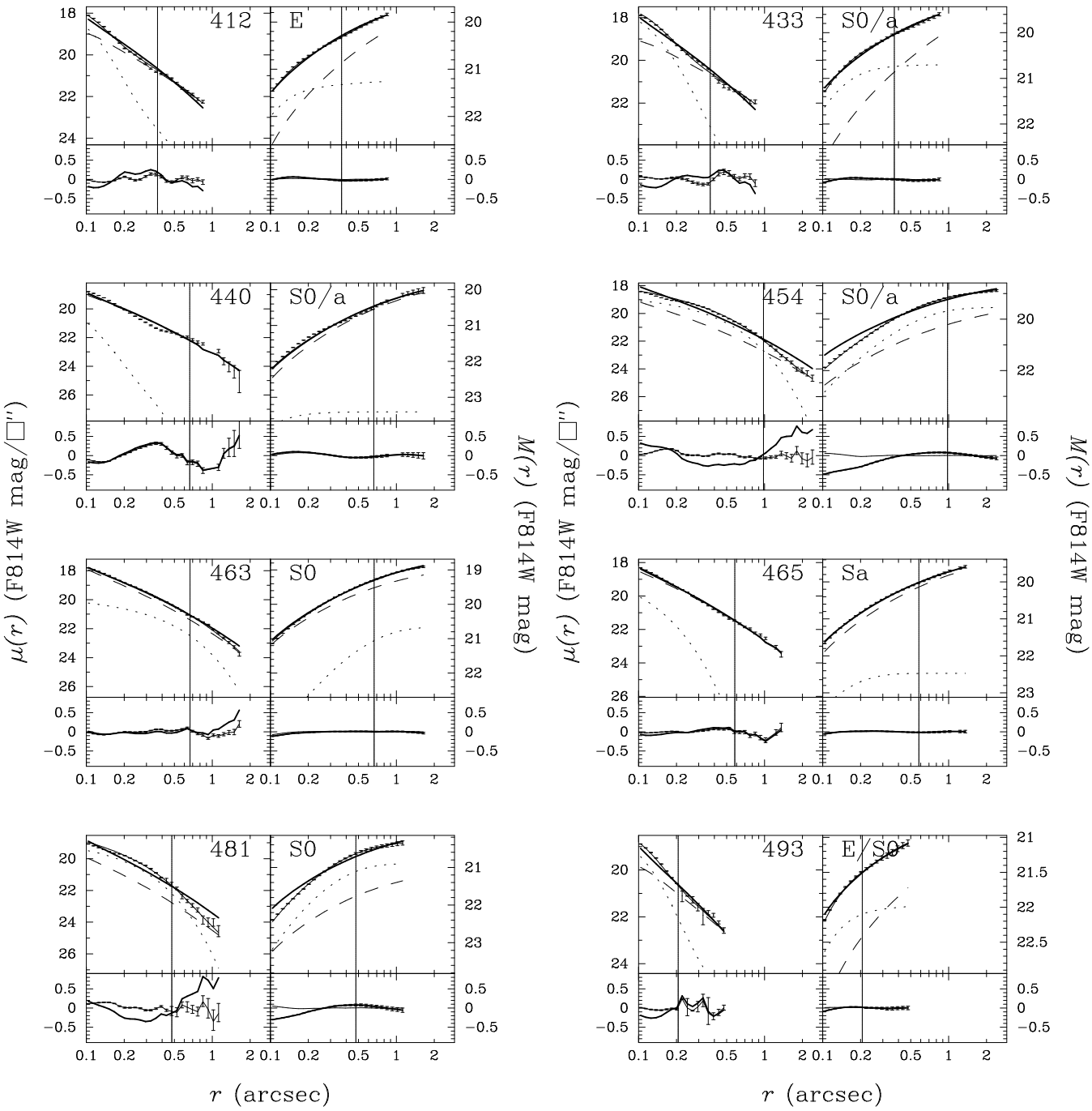

FIG. 3. (continued) —

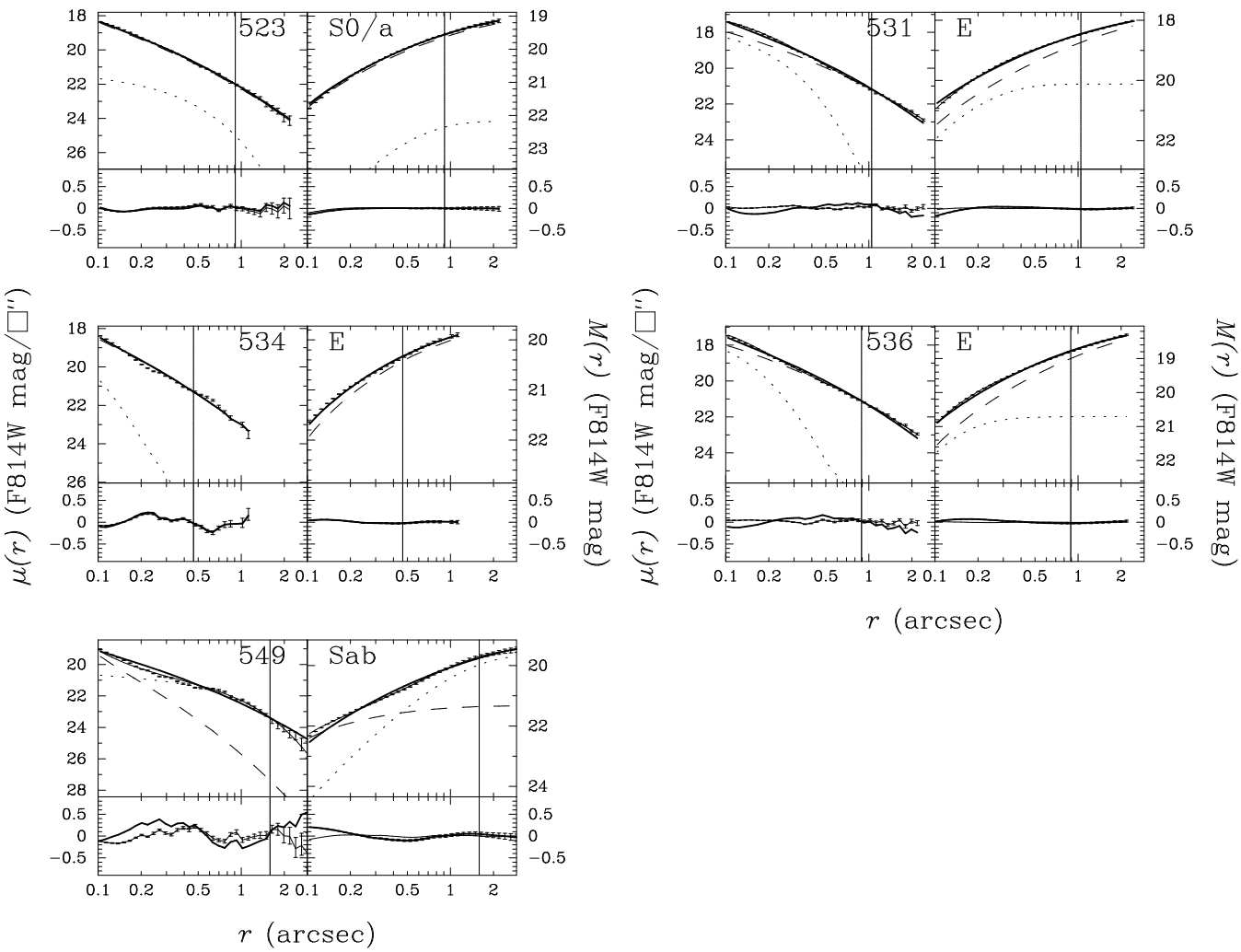

FIG. 3. (continued) —

FIG. 4.— F814W residuals from the $r^{1/4}$-law image modeling. Note the disky residuals in many galaxies. The boxes are $15''$ on each side. The galaxies classified as E+A are ID # 209, 328, and 343. Galaxy # 234 is a star-forming emission line galaxy. Galaxy # 375 is the BCG.

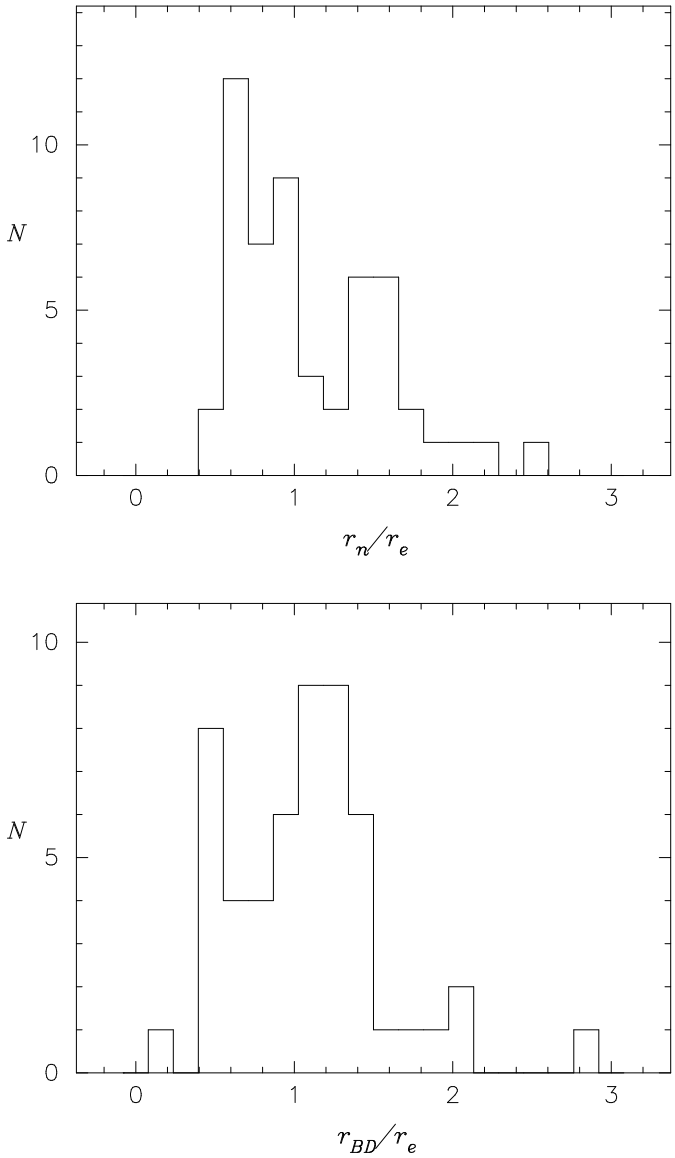

FIG. 5.— (a) The distribution of the ratio of half-light radii, derived from the best-fit $r^{1/n}$-laws, to the half-light radii from the de Vaucouleurs ($n = 4$) fit. (b) The distribution of the ratio of half-light radii, derived from the bulge-plus-disk fits, to the half-light radii from the de Vaucouleurs fit.

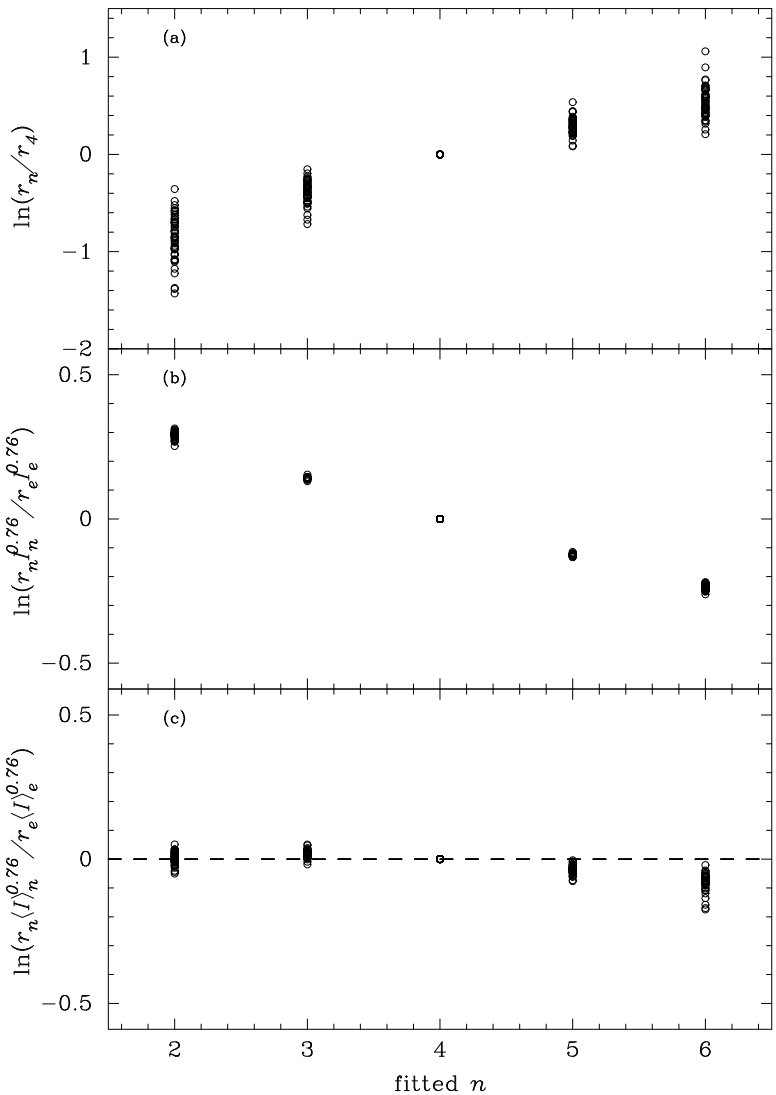

FIG. 6.— (a) The ratio of half-light radii derived from all $n \neq 4$ to the effective radius from the de Vaucouleurs ($n = 4$) fit. (b) The ratio of the effective fundamental plane parameter from these n fits, with the effective fundamental plane parameter from the de Vaucouleurs fit. (c) The ratio of the mean effective fundamental plane parameter from these n fits, with the mean effective fundamental plane parameter from the de Vaucouleurs fit. The data for all 53 galaxies are shown, for every value of n fit.

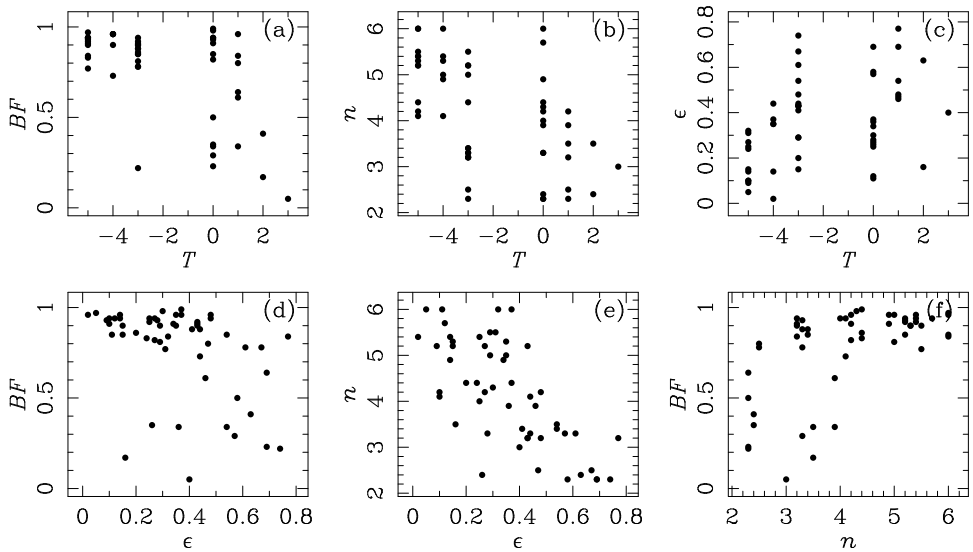

FIG. 7.— (a-c) Bulge fraction, *n*, and ellipticity are plotted against the visual classifications from Fabricant *et al.* (1999). Note that, as expected, visually classified early-types have high bulge fractions and typically have large values of *n*. In (d) and (e) we plot the bulge fraction and *n* against ellipticity. In (f) we compare *n* with *BF* and note that those galaxies which are best-fit using large values of *n* tend to have high bulge fractions.

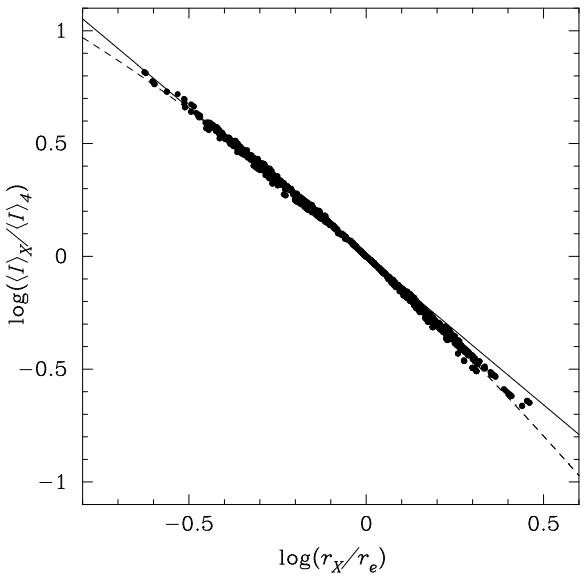

FIG. 8.— For every galaxy in the sample, we show the ratios of $\langle I\rangle_X/\langle I\rangle_4$ vs. r_X/r_4, where X denotes either the $r^{1/n}$-law structural parameters ($n = 1\ldots6$) or the bulge-plus-disk structural parameters. Note that $r_e \equiv r_4$. For this plot, the structural parameters derived from every tested fitting range are used, thus several points exist for each galaxy and profile shape. The solid line indicates the curve of constant $r\langle I\rangle^{0.76}$, running parallel to the fundamental plane. The dashed line is the curve expected for a pure $r^{1/4}$-law growth curve.

This figure "fig1.jpg" is available in "jpg" format from:

http://arXiv.org/ps/astro-ph/9911065v1

This figure "fig4.jpg" is available in "jpg" format from:

http://arXiv.org/ps/astro-ph/9911065v1